

Aerobreakup in disturbed subsonic and supersonic flow fields

T. G. THEOFANOUS, G. J. LI, T. N. DINH
AND C.-H. CHANG

Center for Risk Studies and Safety, University of California, Santa Barbara, CA 93106, USA

(Received 10 February 2006 and in revised form 14 August 2007)

This work concerns the breakup of millimetre-scale liquid droplets in gaseous flow fields that are disturbed from free-stream conditions by the presence of solid obstacles or other drops. A broad range of flow conditions is considered – from subsonic to supersonic, from highly rarefied to ambient pressures, and from fixed cylindrical obstacles to free liquid droplets (as obstacles). The liquid is water or tributyl phosphate, a water-like low-viscosity fluid of very low vapour pressure. We present data on deformation and breakup regimes, and, aided by numerical simulations, we discuss governing mechanisms and the time scaling of these events. Thereby a methodology is demonstrated for conveniently forecasting first-order behaviours in disturbed flow fields more generally. The highly resolved images lend themselves to testing/benchmarking numerical simulations of interfacial flows. These results, along with the experimental capability developed, constitute one of the key building blocks for our overall long-term aim towards predicting ultimate particle-size distributions from such intense aerodynamic interactions involving very large quantities of Newtonian and viscoelastic liquids.

1. Introduction

We are interested in the particle size distributions that result from the breakup of large quantities (tens to hundreds of kilograms) of liquids suddenly exposed to high-speed gas flows. The conditions of practical interest include flow speeds in the km s^{-1} range, gas densities from atmospheric to one-ten-thousandth of it, and Newtonian as well as viscoelastic constitutions. The overall approach has been described in Theofanous *et al.* (2006). Herein we present an evaluation of the role of proximity to other entities in affecting the outcome at the local scale; that is, with the liquid in the form of drops and the other entities also at the mm-scale. This issue of proximity refers to the early stages of dispersal, the therein found dense regime, and the associated multi-body interactions via long-range flow disturbances. However, it is important to note that at large scales this dense regime is also characterized by highly non-uniform (spatially) aerodynamics (large-scale collective behaviour), leading to history effects that can only be captured by coupled system-level descriptions.

Previous work with Newtonian-liquid mm-scale (isolated) drops was at subsonic or mildly supersonic conditions as obtained in shock tubes, and it has been focused on the definition of breakup regime transitions, the principal scaling parameter being the Weber (We) number (Gelfand 1996; Theofanous, Li & Dinh 2004). There are also data on the effect of viscosity on the critical We for breakup (Hinze 1955; Hanson, Domich & Adams 1963; Brodkey 1969; Hsiang & Faeth 1992), and a few

data on the general visualization of viscoelastic drops at very high We flows (Matta & Tytus 1982; Joseph, Beavers & Funada 2002). The effect of viscosity scales with the Ohnesorge (Oh) number, and it becomes important when $Oh > 10^{-1}$. Faeth and co-workers (Hsiang & Faeth 1992; Chou, Hsiang & Faeth 1997; Chou & Faeth 1998; Dai & Faeth 2001) and Gel'fand, Gubin & Kogarko (1974) reported data on daughter-drop size distributions for low and intermediate Weber numbers ($We < 400$), and Villermaux, Marmottant & Duplat (2004) for mm-scale jets in coaxial gas flows.

In this work, we consider two-body configurations involving a solid fixed cylinder with a drop placed behind it, or two free drops. Emphasis is placed on in-line (with the flow) arrangements, but a few staggered arrangements are also examined. The free-stream field is uniform and steady at speeds that include subsonic and Mach 3 conditions, at near atmospheric and rarefied pressures, respectively. The liquid used in the low-pressure tests is tributyl phosphate (TBP), a Newtonian fluid of sufficiently low vapour pressure but otherwise water-like (density–viscosity–surface tension: 978 kg m^{-3} – 4cP – 0.027 N m^{-1}). At normal pressures we employ distilled water (1000 kg m^{-3} – 1 cP – 0.07 N m^{-1}). In all cases, viscous effects are negligible ($Oh < 10^{-1}$).

A principal objective is to determine and elucidate mechanisms of pattern formation (flow regimes) in deformation and breakup, along with associated timings. A subsidiary aim is to create a wider database (than that found in single-drop experiments) for understanding the physics of deformation, interfacial instability and breakup, so as to gain an entry into the behaviour of non-dilute systems. A further latent purpose is to make available highly resolved images of interfacial evolutions that are suitable for testing/benchmarking predictions of numerical simulations that include full interfacial dynamics (Nourgaliev, Dinh & Theofanous 2006; Theofanous *et al.* 2006; Nourgaliev & Theofanous 2007). Recent data and analysis with single drops in a free stream (Theofanous *et al.* 2004; Theofanous & Li 2007) will be used as a point of reference in examining the data reported herein.

2. The ALPHA-II facility and definition of experiments/parameters

The base flow field is generated in a pulsed supersonic wind tunnel called the ALPHA-II facility (Li *et al.* 2003). As illustrated in figure 1, the facility consists of two tanks connected with a flow channel that incorporates a converging–diverging nozzle. For the supersonic flow tests reported here this was a Mach 3 nozzle. The flow is initiated by rupturing a diaphragm, and as long as the initial pressure ratio is over 37, the flow obtained is Mach 3 ($\sim 620 \text{ m s}^{-1}$), at a static pressure that is the $1/37$ of the pressure level in the supply tank. The supply and receiving volumes are such that under the most extreme conditions the flow is steady for durations of ~ 100 ms at a minimum. The receiving volume can be evacuated down to a few tens of Pa (~ 0.1 millibar) which defines the lower bound of the static pressures achievable. In the [Mach number]–[dynamic pressure] space, the accessible region (figure 2) can be obtained by selecting an appropriate nozzle, as required. The flow channel, 4 m long, $0.2 \times 0.2 \text{ m}^2$ in cross-section, is transparent and fully accessible to visualization.

The flow field in the channel was mapped by means of piezoelectric measurements of stagnation pressures (P_s) for the range of operating conditions (at $M = 3$) down to 10 Pa. The flow was found to be close to ideal, with rise times of less than 0.5 ms, steady with minimal fluctuations, absent ‘diamond patterns’ due to shock reflections, uniform in the central $\sim 80\%$ of the channel cross-sectional area, and quantitatively in agreement with theory (figure 3). For the subsonic flow runs the ALPHA was employed at very low pressure ratios (1.03 to 1.35). Flow velocities were deduced

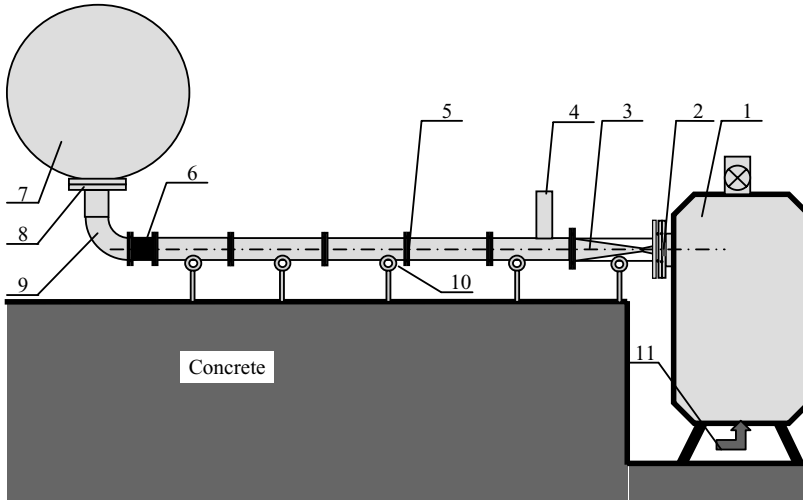


FIGURE 1. Schematic of the ALPHA-II facility. 1, supply tank; 2, diaphragm holder; 3, nozzle; 4, drop generator; 5, test section; 6, bellows; 7, receiver tanks.

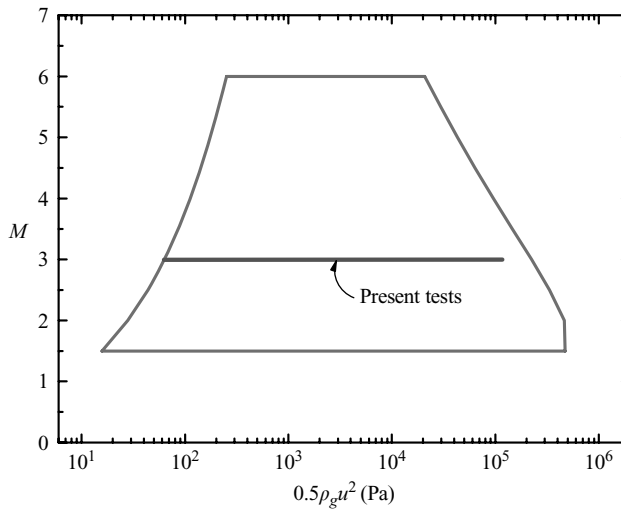


FIGURE 2. Experimentally accessible region in the ALPHA-II facility.

from the shock speeds (measured by two piezoelectric transducers 3.2 m apart), and their magnitude was selected by adjusting the pressure level in the supply tank, the receiver being always at atmospheric pressure.

In all tests, the gas (dry air) temperature in the supply tank was 295 ± 2 K, so that in all Mach 3 flows, the gas velocity was 622 m s^{-1} . As indicated by the consistency with theory in figure 3, uncertainties in the gasdynamics at supersonic conditions are negligible. For the subsonic flow tests, the potential error in flow speed owing to errors in shock speed measurement is less than 7%.

The experiment concept is based on the idea that within the fragmentation time, the main liquid mass displacement is minimal and this allows high-magnification observation of the deformation, instability and entrainment processes – seeing the

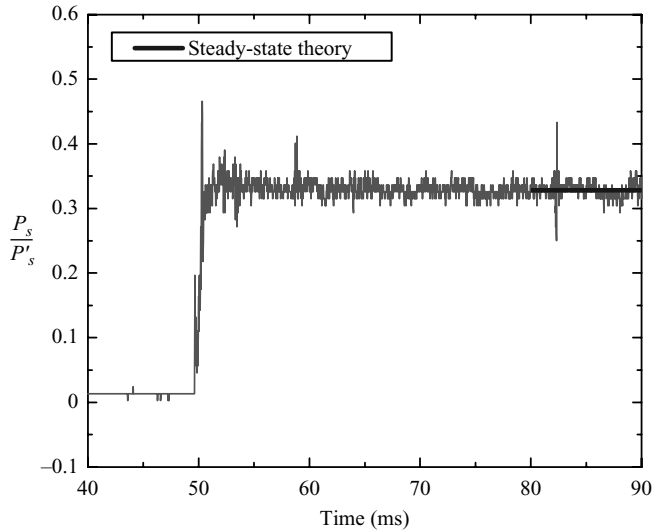


FIGURE 3. Typical stagnation pressure data in the ALPHA-II facility. The short straight line shows the theoretically predicted value. P'_s is the supply tank pressure.

fragmented masses as they are being generated. We have also demonstrated that downstream visualization sampling of the fine mist moving at speeds of hundreds of metres per second is possible to the extent that allows accurate determination of particle-size distributions. This was demonstrated also for viscoelastic liquids for which the breakup process evolves to a degree that makes far downstream observation essential (Theofanous 2005).

Visualization is performed by two Phantom V7 high-speed digital cameras, while illumination is provided by a 20 W copper-vapour laser (Oxford Lasers, LS20-50); ~ 10 nanosecond light pulses synchronized at rates of up to 50 kHz with the cameras. The cameras can be run independently at rates of up to 160 kHz, and the laser can provide single or double pulses of light for still large-format photography, which is employed when there is a need to sample comprehensively the particle cloud far downstream. In the experiments discussed here, we focus on the near field (typically up to ~ 10 drop diameters). The 10 ns exposure times provide an enhancement of spatial resolutions (reduction of motion-induced blur) by more than one order of magnitude in comparison to previous work on drop breakup (typically done at exposures of ~ 300 ns or more).

The liquid release mechanism, located near the channel entrance (figure 1), varies with the quantity and type of liquid involved, and also with the drop-configuration being examined. Here we have drop-cylinder and drop-drop configurations, as noted already mostly in-line, and at separation distances mostly of 2 and 4 diameters as shown in figure 4. A few runs were also made at $10 L_x/D$ (Series C-D3.C) and some at off-set (staggered) arrangements (Series C-D3.D and E). The nomenclature in this figure will be used to identify runs in the remainder of this paper.

In an experimental run, all actions are automatically sequenced so that the drop(s) can be caught within the field of view of the camera(s) at the requisite magnification, from the initial instant of its interaction with the gas flow. The data are then transferred to a computer where they are processed according to the purpose of the

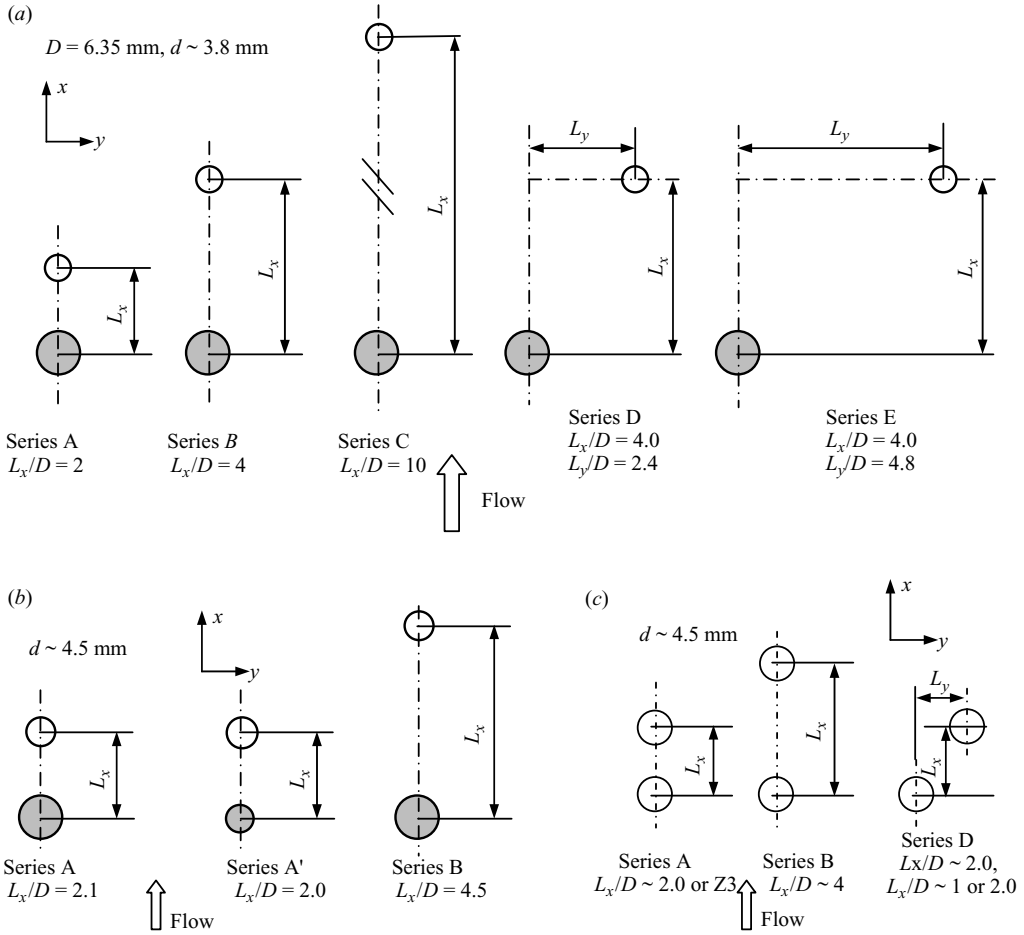


FIGURE 4. Geometric configurations considered: (a) Drop behind a rod in supersonic flow (C-D3); (b) Drop behind a rod in subsonic flow (C-D0); (c) Two drops in subsonic flow (D-D0). D , rod diameter; d , drop diameter.

test. Here we focus attention on the pattern and timing of deformation, the character of the interfacial instability, and mode and timing of breakup.

As noted above, the principal scaling parameter is the Weber number (We). It has been defined as 8 times the ratio of the dynamic pressure ($0.5\rho_g u^2$) exerted by the flow on the forward stagnation point of the drop, to the surface tension pressure ($4\sigma/d$), where ρ_g is the gas density and σ is the interfacial tension coefficient. In this definition, at breakup this ratio is ~ 1 and the critical Weber number $We_{CR} \sim 8-12$ (Hanson *et al.* 1963). In subsonic flow u is the free-stream velocity, and static pressure changes around the drop are modest. In supersonic flow, the static pressure varies greatly with position, and it is the full stagnation pressure (P_s) behind the bow shock that is required in order to preserve the concept of destabilizing force in the Weber number for this case. Thus on an equivalent basis:

$$\frac{P_s d}{4\sigma} \approx \frac{\gamma M^2 d}{4\sigma} P_\infty = \frac{1}{4} \frac{\rho_g u^2 d}{\sigma} = \frac{We}{4}, \quad (2.1)$$

where γ is the gas specific heat ratio, and P_∞ is the static pressure in the free stream. In supersonic flow, the critical $We \sim 26$ (Theofanous *et al.* 2004), which indicates that the critical value of the ratio is 6.5; that is, only slightly lower than that in the subsonic case.

The drop/rod (gas) Reynolds numbers are defined in terms of respective diameters (d/D) and the free-stream velocity, density and viscosity:

$$Re = \frac{\rho_g u d}{\mu_g} = \sqrt{\frac{\gamma}{RT_0}} \frac{Md}{\mu_g} P_\infty, \quad (2.2)$$

where R is the gas constant, and T_0 is the free-stream temperature. For the drop/rod length scales found in these experiments, the Reynolds numbers are within a factor of 1.7 of each other. As noted already, the effect of liquid viscosity is reflected by the Ohnesorge (Oh) number:

$$Oh = \frac{\mu_l}{(\rho_l \sigma d)^{0.5}}, \quad (2.3)$$

where μ_l/ρ_l is the liquid viscosity/density. For all present experiments, $Oh < 10^{-1}$. Finally, in the presentation of our data we will make use of a time scale defined originally in Engel (1958) through consideration of the physics involved in drop deformation in subsonic flow,

$$t^+ = \frac{d}{u} \sqrt{\frac{\rho_l}{\rho_g}} \quad \text{so that} \quad T = t/t^+. \quad (2.4)$$

This provides a good point of reference to begin with since as a general rule from the literature on isolated drops, the breakup time has been taken as $T \sim 5$. The definition of breakup time and related time scales are discussed in §7.

3. Summary of recent isolated-drop results

The key points we wish to make can be expressed with the help of figures 5, 6 and 7. These data were obtained in ALPHA, with fluids and conditions similar to those of interest here, still for $Oh < 0.1$, but reaching high enough We so as to delineate the main regime transition (for isolated drops) as explained below. These data benefit from the increased space–time resolution of the present visualization equipment, and also from the quasi-three-dimensional rendering made possible by the laser-induced fluorescence (LIF) technique – the latter was found to be not necessary for the present experiments, as it will become clear in the next section.

The key and common feature of the breakups seen in figure 5 is that they occur as a result of the gas going through the drop. The regimes seen in the top two rows are known from previous works with subsonic flows, and their names have been established as bag and bag-and-stamen (or umbrella), respectively. The multi-bag and multi-wave regimes seen in the bottom four rows were found at supersonic ($M = 3$) conditions with low enough densities to compensate for the much higher velocities (see §4). The LIF images (bottom two rows) provide the first clear, quasi-three-dimensional view of the internal breakup structure that has not been accessible via the shadowgraph method (a sample shadowgraph is shown immediately above the LIF). In particular, we note that in this way we can determine when there is complete loss of bodily coherence, which is a key event in the breakup history of a drop. Incidentally, at normal pressure–temperature conditions, $We \sim 75$ would yield the stripping regime (Hsiang & Faeth 1992; Gelfand 1996), see below. Thus, a second-order dependence on the Mach number is also indicated (the first-order one being on

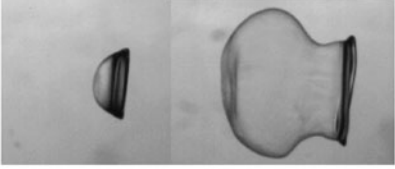
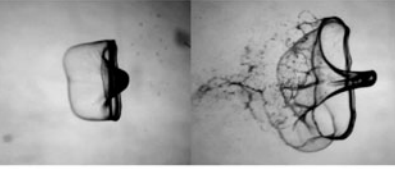
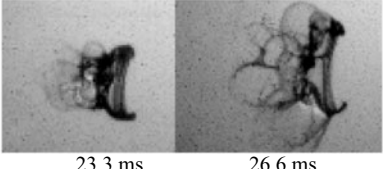
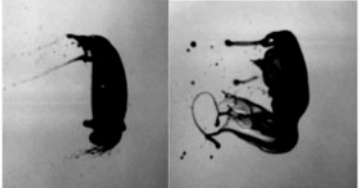
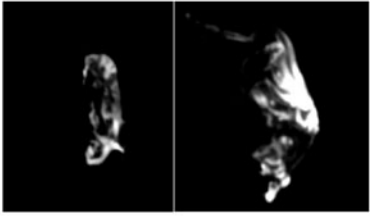
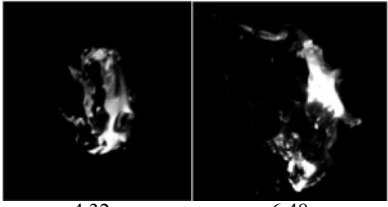
R T P	Bag	 <p style="text-align: center;">11.7 ms 14.6 ms</p>	$We = 7.0$ $t^+ = 8.8 \text{ ms}$ Subsonic
	Bag and Stamen	 <p style="text-align: center;">9.9 ms 11.8 ms</p>	$We = 13.0$ $t^+ = 8.5 \text{ ms}$ Subsonic
	Multibag	 <p style="text-align: center;">23.3 ms 26.6 ms</p>	$We = 27.0$ $t^+ = 7.5 \text{ ms}$ $M = 3$
	Multiwave	 <p style="text-align: center;">4.20 ms 6.30 ms</p>	$We = 75$ $t^+ = 4.3 \text{ ms}$ $M = 3$
	Multiwave	 <p style="text-align: center;">4.32 ms 6.48 ms</p>	$We = 75$ $t^+ = 4.3 \text{ ms}$ $M = 3$
	Multiwave	 <p style="text-align: center;">4.32 ms 6.48 ms</p>	$We = 75$ $t^+ = 4.3 \text{ ms}$ $M = 3$

FIGURE 5. Illustrative samples of the RTP regime from ALPHA-II tests with isolated drops ($d \sim 3.5 \text{ mm}$, different magnifications shown). Bottom two rows are LIF images taken at right angles a , or obliquely b .

the We). The name Rayleigh–Taylor piercing (RTP) has been collectively applied to underline a common origin (the key mechanism) for the instability that drives these four kinds of breakup (Theofanous *et al.* 2004).


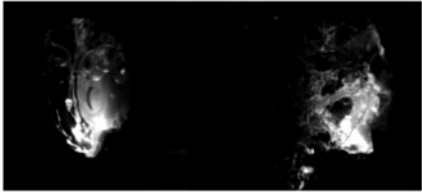
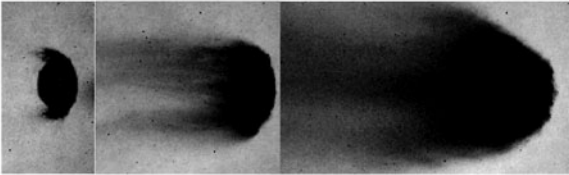
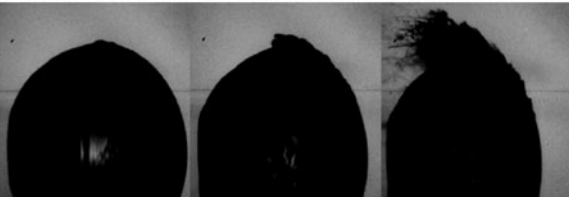
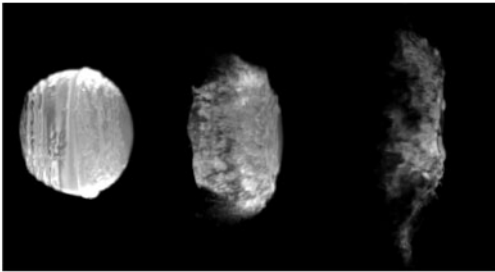
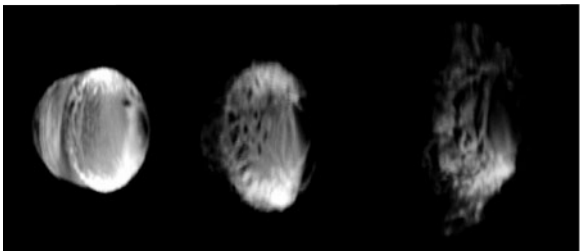
R T P		<i>a</i>	$We = 1000$ $t^+ = 1.2 \text{ ms}$ $M = 3$
		<i>b</i>	$We = 1000$ $t^+ = 1.2 \text{ ms}$ $M = 3$
S I E			$We = 3300$ $t^+ = 0.67 \text{ ms}$ $M = 3$
			$We = 2500$ $t^+ = 0.77 \text{ ms}$ $M = 3$
		<i>a</i>	$We = 5400$ $t^+ = 0.49 \text{ ms}$ $M = 3$
		<i>b</i>	$We = 5400$ $t^+ = 0.51 \text{ ms}$ $M = 3$

FIGURE 6. Illustrative samples of SIE regime, and of the RTP-to-SIE transition (top two rows) from ALPHA-II tests with isolated drops ($d \sim 3.5 \text{ mm}$, different magnifications shown). Top and bottom two rows are LIF images taken at right angles *a*, or obliquely *b*.

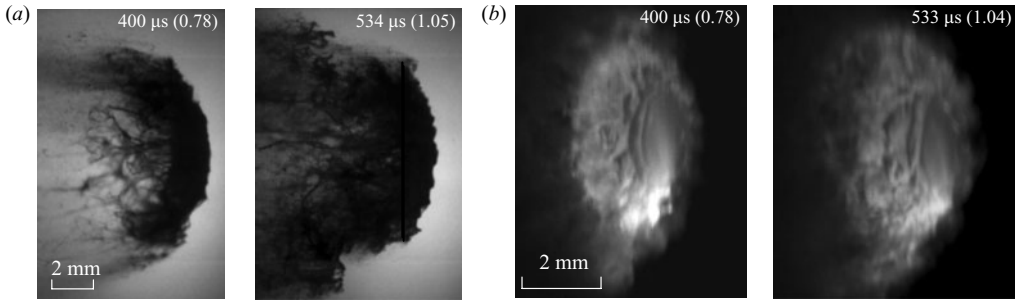


FIGURE 7. Comparison of shadowgraph and LIF images in SIE regime. (a) Shadowgraph; (b) LIF images, taken obliquely. Images were taken from ALPHA-II tests with isolated drops ($d \sim 3.5$ mm). The numbers in parentheses are dimensionless times, normalized by t^+ .

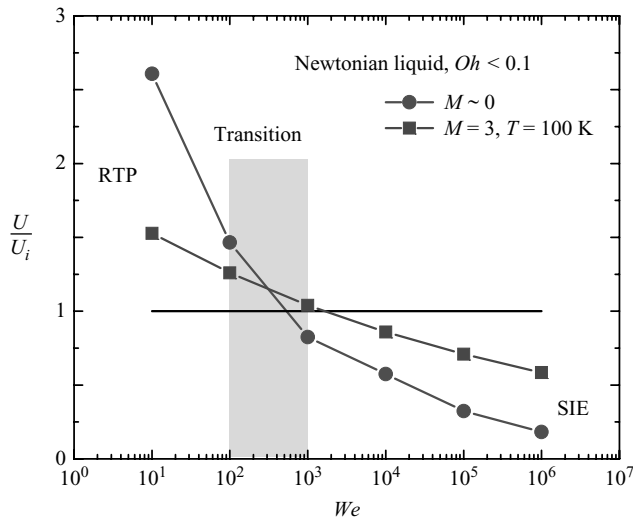


FIGURE 8. Theoretical breakup regimes. U is the R–T wave penetration velocity in the nonlinear regime; U_i is the shear-induced circumferential velocity on the liquid surface.

Starting at $We \sim 10^2$, shear begins to become important, and co-participate with RTP in the breakup process, as illustrated in figure 6 (top two rows), with increasing influence, until at about $We \sim 10^3$ the shearing action appears to take on the dominant role (A rough theoretical interpretation of this transition is shown in figure 8). This can be seen in figure 6 (bottom two rows), as a major redistribution of the liquid mass into a fragmenting (but macroscopic, not misty) ‘sheet’ extending out with a significant radial velocity, a phenomenology that has eluded shadowgraph imaging (middle two rows). On this basis we can now understand why the stripping mechanism (Taylor 1949; Ranger & Nicholls 1969) fell short in explaining the rates of breakup seen experimentally.† Moreover, as we can see in the LIF images, the conceptual basis

† As detailed by Rienecke *et al.* (1975), Ranger & Nicholls (1969) found and corrected an error in Taylor’s algebra, but they too appear to have committed an error (it seems to be of arithmetic origin), thus overestimating the stripping rate by about an order of magnitude. We have checked these calculations and agree that stripping would produce complete atomization in $T \sim 40$ instead of the experimentally found $T \sim 5$.

of the stripping model is not what is actually happening at $We > 10^3$. This early loss of coherence also explains why Reinecke & Waldman (1970) were unable to relate their (and Engel's) data to the physics of deformation of a coherent drop as proposed by Burgers (1958), or by several alternatives of their own. It seems necessary to make the distinction from stripping, thus we use the term 'shear-induced entrainment' (SIE) to describe this breakup regime.

For completeness we should also note that it has been proposed that at much higher values of the We there is yet another transition to a regime called 'catastrophic', a term coined by Reinecke & Waldman (1970) (more readily available in Waldman, Reinecke & Glenn 1972) to describe the sudden disappearance of a fragmenting (by stripping) drop. In particular they state that:

Examination of the shadowgraphs demonstrated conclusively that material was being stripped from the drops continuously at all test conditions. At the more severe test conditions, a second, 'catastrophic' mode of breakup became dominant, and the drop was shattered before all its material could be removed by stripping. The catastrophic mode of breakup is related to the unstable growth of waves on the front surface of the drop caused by the rapid acceleration of the drop by the air stream. In this mode, surface waves are observed to grow rapidly until their amplitude is comparable to the dimensions of the drop, at which point the drop is torn apart,

and further-on that:

transition from the stripping mode of breakup to catastrophic breakup occurs early in the tests at a shock Mach number of 11, at intermediate time at Mach 6, and at late time (if at all) at Mach 3

The corresponding We for these tests were $\sim 10^6$, 2.5×10^5 and 8×10^4 respectively, and the 'early', 'intermediate' and 'late' timing of this event correspond to T -values of 1.4, 2.0 and 2.7, respectively. The suggestion found experimental support[†] from Simpkins & Bales (1972), and theoretical support from Harper, Grube & Chang (1972); however, it should also be noted that the validity of this mechanism remains far from clear because: (a) the interpretations of these experiments were heavily compromised by ignoring the extremely high gas temperatures (reaching up to 3 300 and 11 000 K for Mach 6 and 11, respectively), and (b) the theory did not take into account the shearing action of the gas flow.

4. The cylinder-drop configuration (C-D3 and C-D0) runs

A total of 45 experiments were carried out with the cylinder-drop configuration, both in Mach 3 and subsonic ($M < 0.11$) flows, as summarized in table 1. The choice of conditions was made in the course of the work so as to focus on areas with strongly identifiable deviations from isolated drop behaviours. This produced an emphasis on Series A and B runs as seen in table 1. In §§ 6 and 7, we show how these

[†] The idea was re-morphed by Joseph, Belanger & Beavers (1999) who claimed to have seen in their shadowgraphs the Rayleigh-Taylor waves responsible for catastrophic breakup, and claimed that they had quantitative agreement (the images they show for this 'measurement' were taken at $T \sim 1$) with the most dangerous wavelengths predicted from standard linear stability analysis. However, these results at shock Mach numbers of 2 and 3 (We of 10^4 and 2×10^4 , respectively): (a) are not consistent with the evidence of Waldman *et al.* (1972) and (b) are not supported by our LIF data which allow unambiguous visualization of the frontal surface area of the drop. This latter aspect can be seen by contrasting with the $T \sim 1$ shadowgraph and LIF images in figure 7, and noting that the 'waves' are an artefact of the projection involved in the shadowgraphy method.

	Series A	Series A'	Series B	Series C	Series D	Series E
$Mach = 3$	$L_x/D = 2$		$L_x/D = 4$	$L_x/D = 10$	$L_x/D = 4$	$L_x/D = 4$
$d = 3.8$ ± 0.1 mm	5 runs		5 runs	4 runs	$L_y/D = 2$	$L_y/D = 5$
$D = 6.35$ mm	$We = 45-491$		$We = 43-483$	$We = 79-304$	5 runs	5 runs
$T_0 = 107$ K	$Re =$ 300-3300		$Re =$ 300-3200	$Re =$ 500-2000	$We =$ 43-485	$We =$ 45-305
$u = 622$ m s ⁻¹					$Re =$ 300-3200	$Re =$ 300-2000
$Mach \sim 0,$ $d = 4.0$ ± 1 mm	$L_x/D = 2$ 8 runs	$L_x/D = 2$ 7 runs	$L_x/D = 4$ 6 runs			
$P \sim 10^5$ Pa	$D = 6.35$ mm	$D = 3.96$ mm	$D = 6.35$ mm			
$T_0 \sim 300$ K	$We = 6-121$	$We = 7-121$	$We = 6-121$			

TABLE 1. Specification of the C-D3 and C-D0 runs.

long-range effects (due to disturbances in the flow fields) can be understood, and in fact be approximately predicted with the help of simple numerical simulations of the aerodynamics in fixed multi-body configurations. Thus, we shall be also able to infer ranges of influence, including any other arrangements such as those considered in a scoping manner in Series C, D and E runs at Mach 3.

An overall perspective on deformation and breakup regimes found in these C-D tests can be obtained from figures 9 and 10, covering the supersonic and subsonic conditions, respectively. Complete time-resolved sequences for most runs excerpted in these two figures can be found in the Appendix. In all discussions that follow, a run is specified in a way that establishes its connection to the complete definition given in table 1. For example ‘run C-D3.B(80)’ is a Mach 3 run, in the cylinder-drop configuration, with an $L_x/D = 4$, and at $We = 80$. Then from the value of We and the drop diameter (3.8 mm) one can find the gas density, and from the temperature (~ 107 K in this Mach 3 case) one can find the free-stream pressure.

The key features found in figures 9 and 10 are two new (in relation to isolated drops, see figures 5 and 6) patterns of deformation and breakup: bullet-like shapes stretching in the flow direction, and flattened structures aligned both with the cylinder axis and with the flow. The other key difference is that in all cases, the resulting particle length scales are considerably larger than those found in corresponding (same We) obstacle-free flow conditions. In supersonic flows such ‘sheltering’ effects may extend out to $L_x/D \sim 10$.

In supersonic flows, the demarcation between these two new patterns is around $We \sim 100$. Well below this value, elongations of the bullet-like structures are modest and the drops remain deformable but stable. At $We \sim 80$, there is out-stretching and eventually entrainment off the trailing tip. At $We = 150$ (the actual onset would be somewhere in the range 80–150) the flattened structures partition into multiple filaments connected by membranes all stretching out in the flow direction. Eventually, the membranes burst and the outstretched filaments entrain off their trailing tips, until there is sufficient time for breakup to occur over the whole body by capillary instability. As seen in run C-D3.A(500), these processes intensify with increasing We . This run also provides direct evidence of the role of counter-rotating vortices that form behind the cylinder – starting at ~ 7 ms, the liquid mass is seen to translate upstream to eventually (at 14 ms) make contact with the cylinder.

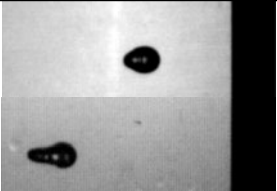
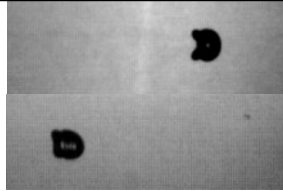
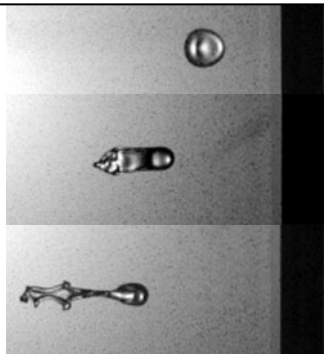
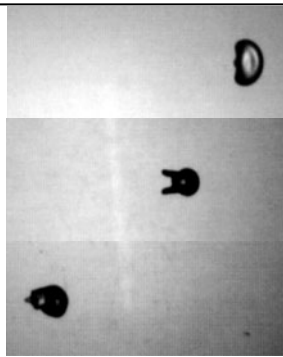
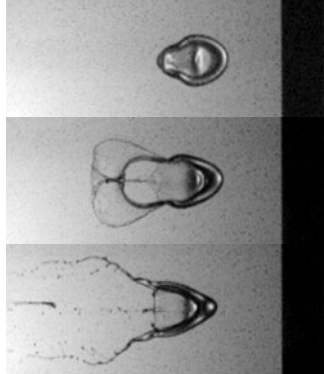
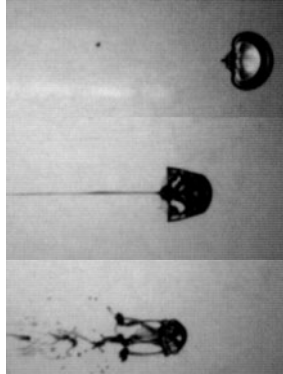
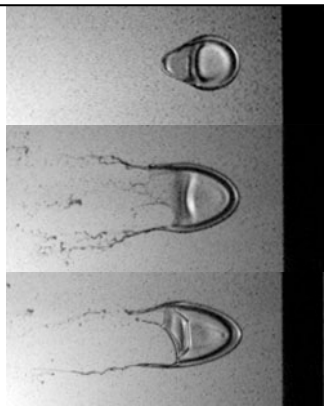
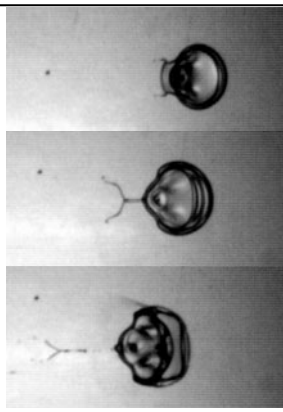
45		25.0 ms 47.0		23.0 ms 43.0
80		9.6 28.8 33.6		12.0 23.0 37.0
150		11.1 13.9 16.7		9.0 19.0 23.0
300		5.6 11.1 13.9		7.0 9.0 11.0
<i>We</i>	C-D3.A		C-D3.B	

FIGURE 9. Summarization of breakup patterns for a drop found behind a cylindrical obstacle in supersonic flow. The characteristic times t^+ for We of 45, 80, 150 and 300 are 6.6, 5.0, 3.6 and 2.6 ms, respectively.







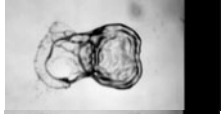


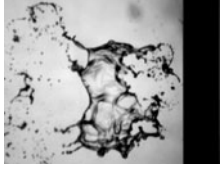

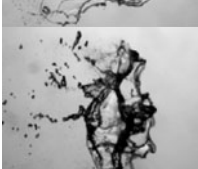
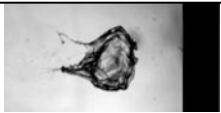
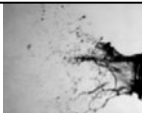

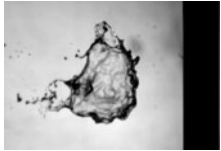
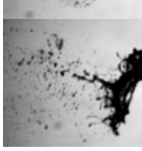
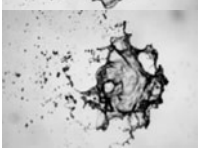






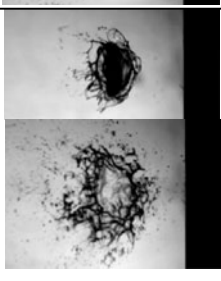
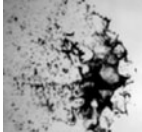
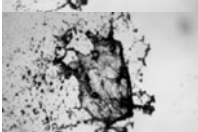
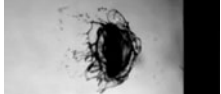


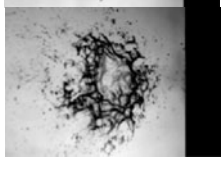
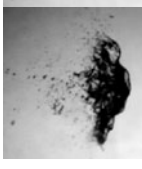
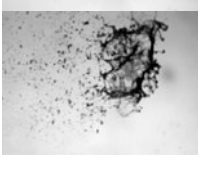
~ 7		14.6 ms		14.2 ms		14.2 ms
		20.4		27.8		20.1
~30		9.4		8.9		9.2
		14.2		11.7		14.0
50		7.2		7.2		7.2
		9.0		9.6		9.0
78		5.6		5.3		5.4
		6.9		6.8		7.0
		6.9		8.2		9.0
120		4.2		4.2		4.0
		5.6		5.6		5.6
<i>We</i>	C-D0.A		C-D0.B		C-D0.A'	

FIGURE 10. Summarization of breakup patterns for a drop found behind a cylindrical obstacle in subsonic flow. The characteristic times t^+ for We of 7, 30, 50, 78 and 120 are approximately 16, 8.5, 6.5, 4.7, 3.9 and 3.3 ms, respectively.

In all supersonic, Series A runs ($L_x/D=2$) the behaviour, although complex and varying in detail with small changes in We , is perfectly regular and reproducible in all fine features – see for example runs C-D3.A(150) and (300). At $L_x/D=4$, the behaviour is similar, but even more rich, as regular wave patterns develop on the body of the membrane itself [runs C-D3.B(150),(300) and (500)], but the breakup is now more abrupt as it involves the whole structure at once, that is, both the filaments and the membranes, especially at the higher Weber numbers.

In subsonic conditions, the new patterns (bullet-like shapes and flattened structures) are essentially the same, but the demarcation is now found at $We \sim 10$. Even though this transition to unstable behaviour and breakup is the same as for isolated drops, the morphologies are completely different in both the below (stable) and the above (unstable) regimes. The other key distinction with the supersonic flow cases described above is that here both filaments and membranes appear to be much more unstable and short-lived. Indeed, the breakup process, rather than gradual and prolonged, can be better characterized as shattering, an abrupt and chaotic disintegration into a cloud of similarly sized particles.

At a finer detail of observation, within transition regions, we can see a co-participation of the basic trends that characterize the individual regimes, stretching and flattening, but also an apparent competition with a flattening in the normal-to-flow direction, as seen with isolated drops. For example, in run C-D3.A(80), we see an initial attempt to flatten, which, however, is overtaken by an axisymmetric squeeze into a bullet-like shape, and this is followed by continuing stretching and breakup of the trailing edge. In runs C-D3.B(43) and (80) on the other hand, an initial trend similar to an isolated drop (flattening in the normal to flow direction), gives way to axisymmetric and/or flattened (in the parallel to flow direction) structures. The same can be seen in all runs C-D0.A and B.

As is the case for isolated drops, our interest in these deformation and breakup patterns is due to their effect on the timing of breakup and the resulting particle size distributions. The latter are quantities that we must learn enough about, so they can be estimated in the intended system-level calculations involving large liquid masses, as mentioned in § 1. In this perspective, the quantitative features of the present results can be summarized in terms of two kinds of reduced results: (i) deformation as a function of time, and (ii) timing at which a drop lost all coherence. The former is represented by the evolutions of the vertical and horizontal diameters as functions of time – they were measured from the time-resolved data such as those shown in the Appendix, and they are presented in terms of appropriate time scales in § 7. From these results we also obtain an estimate of the ‘deformation time’ as discussed also in § 7. The definition of the latter (the ‘breakup time’) requires significant elaboration, and this along with the reduced data are presented in § 7.

5. The drop–drop configuration (D-D0) runs

A total of 15 experimental runs were conducted with the drop–drop configuration, all at near atmospheric pressure, subsonic flow conditions as summarized in table 2. An overall perspective on deformation and breakup regimes found in these *D-D0* tests can be obtained from figure 11. Complete, time-resolved sequences for most runs excerpted in this figure can be found in the Appendix. We follow the same procedure in naming of runs and figures as that described in the previous section.

The description of the deformation and breakup patterns observed will be given in terms of three time periods (figure 12) and identified as follows: an initial, short

	Series A	Series B	Series D
$Mach \sim 0$,	$L_x/D = 2$	$L_x/D = 4$	$L_x/D = 2, L_y/D = 1$
$d = 4.9 \pm 0.4$ mm	$We = 6 - 125$	$We = 6 - 125$	$L_x/D = 2, L_y/D = 2$
$P \sim 10^5$ Pa	$Re = 3000 - 13\,000$	$Re = 3000 - 13\,000$	$We = 7 - 125$
$T_0 \sim 300K$	6 runs	3 runs	$Re = 3000 - 13\,000$
			6 runs

TABLE 2. Specification of the D-D0 runs.

period of minimal interaction between the two drops, a main period characterized by strong long-range interactions, and a final period of coalescence and continuing breakup as a combined collection of liquid masses. In basic terms, the breakup behaviours of the interfered-with trailing drops during the first and second periods are axisymmetric versions of those found in the cylinder–drop configurations. The phenomena of the last period were observed in all experiments in this class, including separation distances of up to $L_x/D = 4$, and staggering of up to $L_y/D = 2$.

In the initial period, the drops respond independently of each other, and as if they were alone (isolated) in the flow field. In particular, we can see flattened structures such as those that are the precursors to Rayleigh–Taylor piercing (RTP) of isolated drops as illustrated in figure 5. At the upper end of the range investigated ($We \sim 65$), we can also see the initial hints of shearing coming into play (backward bending at the edges).

With flattening, the downstream influence of the leading drop increases, thus producing the significant interference seen in the second period. While the leading drop continues to deform and break up as if it were alone, the trailing drop is now seen to reverse into a centripetally-deforming mass, an axisymmetric version of the streamwise flattening seen in the cylinder–drop configurations. This is very pronounced at low We , but remains evident even at $We \sim 60$. Moreover, we found that even at a staggering of $L_y/D \sim 1$ (but not at $L_y/D \sim 2$) these shielding effects persist to an extent sufficient to lead to collision of two masses – by the lead drop sweeping into the trailing one. The result is the inception of the third period.

The outcome of the collision in the third period depends on the shape taken on by the leading drop by that time, and this depends on the magnitude of the Weber number. At near-critical values, this shape is a ‘bag’, and the collision amounts to the trailing drop ‘passing through’ this bag, destroying it in the process, while leaving the ‘ring’ essentially untouched, and unaffected. The same occurs at $We = 17$, involving a ‘bag-and-stamen’. Remarkable also is a case where a small satellite drop passed through the bag, creating first a connecting filament, which after a short time broke off, while the bag self-healed, escaping rupture (figure 13). At the high end of the We -range investigated, the leading drop, having undergone RTP, yields a collection of masses that are uniformly distributed, so that following collision, the breakup and dispersal processes proceed in a collective fashion. This ‘mixing’ of events with drops at different stages of breakup leads to distinctly larger particles in comparison to those resulting from isolated drops at comparable Weber numbers.

6. Simulations of base aerodynamics and first-order interpretations

As shown below, the basic qualitative features of the new deformation and breakup patterns found in this work can be understood rather simply. The same is true for






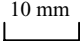



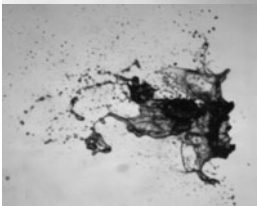
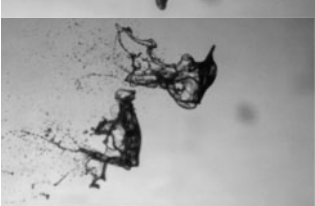
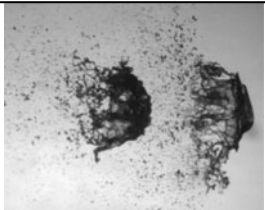



~7		21.0 ms		13.1 ms
		25.0		26.5
12-15		18.5	NA 	
		20.6		
32-40		7.5		4.2
		12.5		8.4
125		5.8		5.4
		7.3		7.9
<i>We</i>	D-D0.A		D-D0.D	

FIGURE 11. Summarization of breakup patterns of two in-tandem drops in subsonic flow. t^+ for We of 7, 16, 38 and 125 are $\sim 16.8, 9.5, 6.4$ and 3.5 ms, respectively.

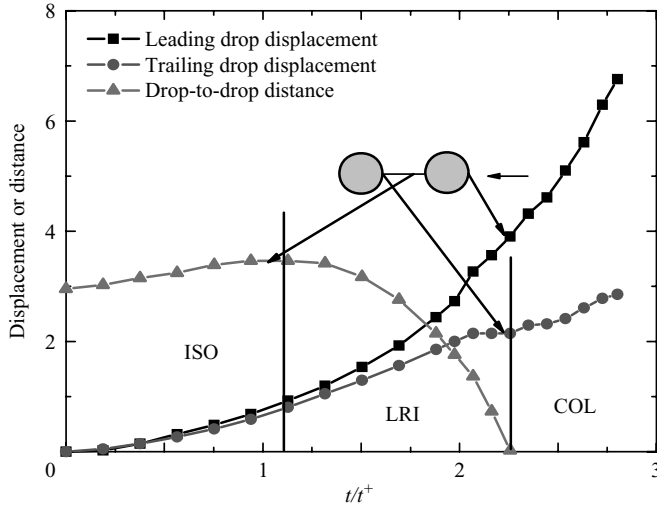


FIGURE 12. Displacements of the two drops and inter-drop distance with time for a run at $We = 6.0$ and $Re = 2880$. Leading/trailing drop diameters 4.91 mm/4.85 mm. Distances are normalized by the leading-drop diameter. ISO represents the first stage with no interference; LRI represents the second stage with strong interference; COL represents the final stage, where the two drops collide. t^+ is the characteristic time for deformation of the lead drop (see § 7).

the different behaviours in subsonic and supersonic flow conditions. In pursuing these qualitative explanations we should also like to consider, as far as possible, quantitative interpretations of regime transitions, the extent of regions of influence owing to the leading body, and associated variations of characteristic time scales for deformation. All these matters we address by means of numerical simulations of the aerodynamics in fixed flow geometries – the methods for fully-coupled simulations are under development (Nourgaliev & Theofanous 2007; Nourgaliev, Liou & Theofanous 2007).

Our calculations were performed with the research code C-UNCLE, a parallel, three-dimensional compressible Navier–Stokes solver, which is an extension of the in-house code UNCLE developed at the University of Kentucky (Chen, LeBeau & Huang 2005). This code is based on a MUSCL-type high-order upwind finite-volume method designed for both structured and unstructured meshes, and it has been tested on several computer clusters, exhibiting high scalability. The Chakravarthy & Osher (1985) TVD scheme, and the implicit Newton-iteration method are used to provide third- and second-order accuracy in space and time, respectively. We also use the AUSM⁺ scheme as the approximate Riemann solver (Liou 1996). It is noted that AUSM⁺ is free of the carbuncle effect, a spurious instability around the forward stagnation area found by other upwind methods, such as Roe’s scheme, at high Mach numbers. Thus, we have a robust and accurate capturing of detached shock waves. Although C-UNCLE had already undergone a series of standard verification tests for inviscid/viscous, subsonic/supersonic flows, we performed additional testing for the geometries (cylinders, spheres), rarefied-flow conditions (down to 10 Pa), and Reynolds numbers (45 to 10^3) of interest here. All these tests were carried out in three-dimensions, and they also provided valuable guidance in optimizing the meshing for the actual calculations of interest. In particular, these tests showed excellent agreement with the detached-shock-position data of Liepmann & Roshko (1957), covering Mach

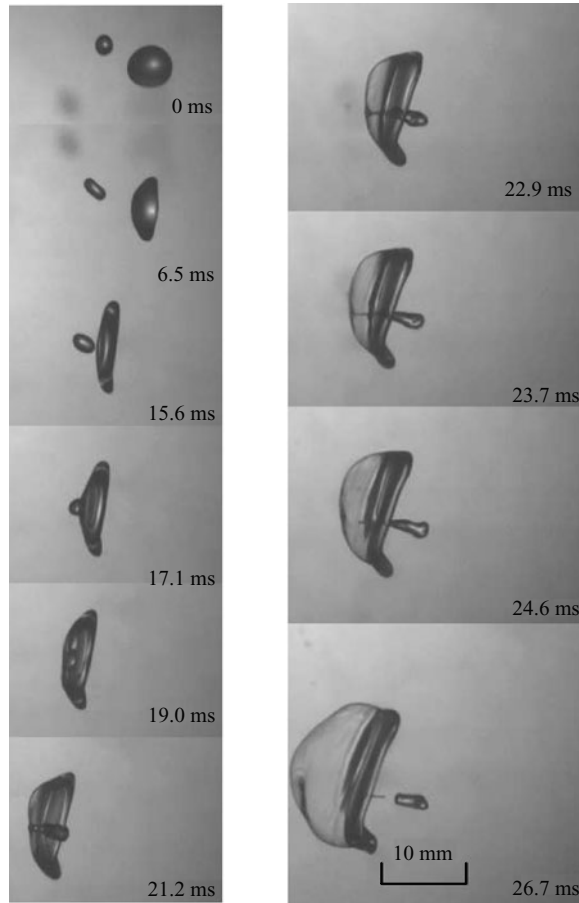


FIGURE 13. A collision event followed by seamless separation. Diameters 2.1 and 4.9 mm. $We \sim 6$, $Re = 2880$ (both based on the large drop).

numbers of 2 to 6, and the Mach 2, drag coefficient data for cylinders (Maslach & Schaaf 1963) and for spheres (Bailey & Hiatt 1972).

All simulations were executed in three-dimensions on a 30-CPU cluster, with meshes of ~ 1 to 2 million cells, requiring 4 to 8 h run time. The computation domain extends from $\sim 8D$ in front of the leading object to $\sim 16D$ behind the trailing one. For the most demanding, supersonic-flow cases, the resolutions in conformal meshing were 160 cells around the cylinder, 120 cells around the sphere, and at least 12 cells within the boundary layer – these were found to be adequate on the basis of the test runs described above. A characteristics-based non-reflecting boundary condition was used on all the inflow/outflow boundaries. Convergence to steady state was ensured by continuing the calculation until the change of drag coefficient between successive steps was less than 10^{-4} times the difference between the first two steps.

As we have seen in the experiments, in this low- to medium- We regime, breakup is preceded by gross whole-body deformation. The latter is the result of normal stresses whose distribution around the drop is sufficient to overcome the capillary stresses. These normal-stress distributions are the simulation results of principal interest here – they provide the means to understand more tangibly the trends found experimentally as discussed below, and they will be further used to extract characteristic drop-internal

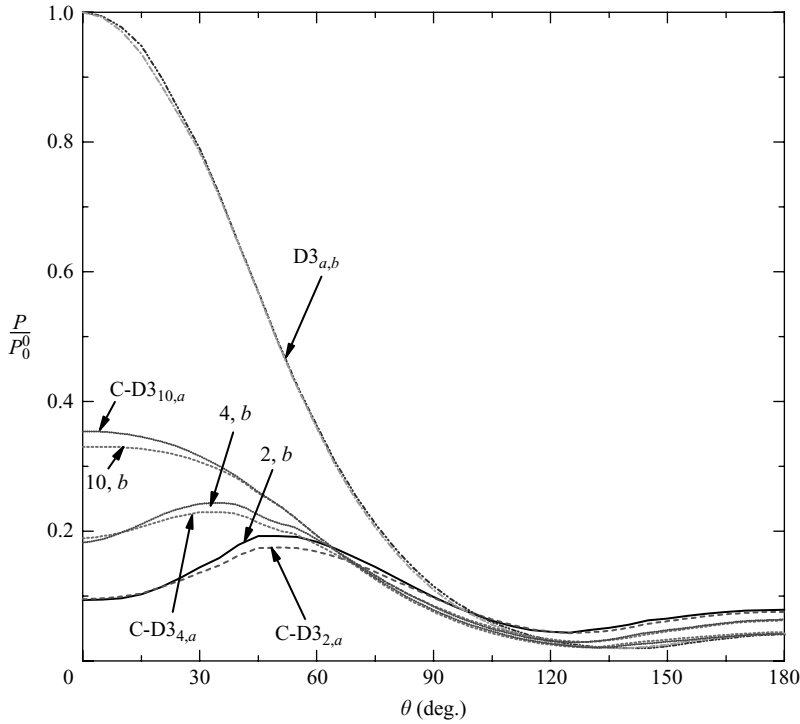


FIGURE 14. Summary of scaled normal stress distributions on the sphere boundary at the intersection with a diametral plane orthogonal to the cylinder. D3 and C-D3 type simulations: $L_x/D = 2, 4, 10$ (subscripts 2, 4, 10); $We = 80, 150$ (subscripts a, b), P_0^0 is 550 Pa and 1032 Pa, respectively.

accelerations and thence times for deformation as explained in § 7. The experimental data also show that shear stresses come into play in the longer term, as shape-changes and increased interfacial area allow enhanced coupling with the gas flow, but since this aspect of the behaviour requires fully coupled simulations, it is left for future study.

In our calculations we considered cases C-D3 and C-D0. In addition we considered isolated spheres, correspondingly called D3 and D0. To cover the conditions of greatest interest (around the main regime transitions), the calculations were carried out for (free-stream) We of 80 and 150 in rarefied supersonic flow, and $We = 28$ in near-atmospheric subsonic flow. The drop-drop-configuration experiments can be understood to some extent as axisymmetric versions of the behaviours discussed on the basis of the cylinder-drop calculations; however, the dynamics will require full gas-liquid coupling, a task currently underway.

The results for all Mach 3 simulations are summarized in figure 14. Several features in these results are relevant to our experimental results and more generally remarkable.

(a) There is a strong ‘sheltering’ effect that extends well into distances of $L_x/D \sim 10$ and beyond. This effect can be more clearly visualized by complete pressure and velocity fields as shown in figures 15 and 16. Note also in these figures the absence of time-dependent secondary motions; that is, there are no trailing vortices found in subsonic flows.

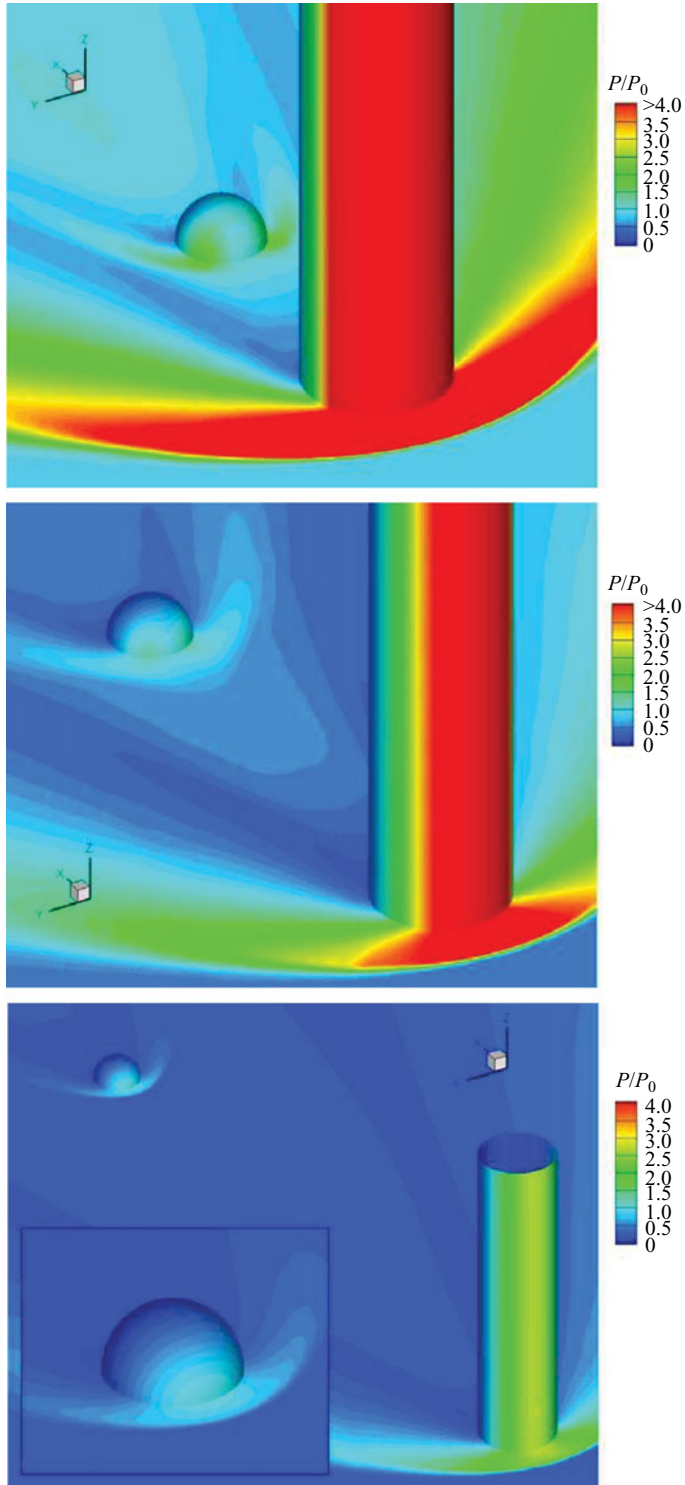


FIGURE 15. Development of the region of influence with varying $L_x/D (= 2, 4, 10)$ in type C-D3 runs. Normal stresses are scaled by the value on the forward stagnation point of the sphere (P_0), 53, 104, and 195 Pa, respectively.

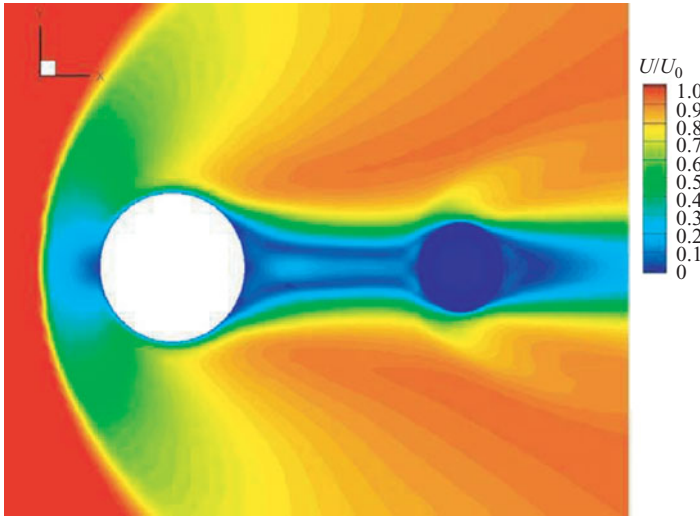


FIGURE 16. Illustration of the induced near-stagnated flow region in the two-body configuration C-D3, $L_x/D = 2$, $u_\infty = 622 \text{ m s}^{-1}$.

(b) This sheltering is accompanied by a sideways shift of the principal stagnation point (point of maximum normal stress). Both the shift and the magnitude of the front-to-sides stress imbalance depend on the sphere-to-cylinder relative position and disappear at $L_x/D \sim 10$.

(c) These effects (underlying distributions) are independent of We .

On this basis we can now see the cause and intensity of flattening seen experimentally (strong at $L_x/D = 2$, not as pronounced at $L_x/D = 4$, and virtually non-existent at $L_x/D = 10$), the order-of-magnitude increase (relative to that of an isolated drop) of the critical We , and the extremely smooth (and reproducible) development of the deformation and breakup processes in all fine detail.

These results suggest a method of rescaling the free-stream We that accounts for the sheltering effect. Based on the actual dynamic pressure acting on the drop (Hanson *et al.* 1963), from figure 14 we have $We_{eff} \sim 0.15 We$, and thus our We -value for the onset of significant deformation and breakup, $We_{CR} \sim 80$, rescales down to the known value of $We_{CR} \sim 10$ found in experiments with isolated drops. In a similar fashion, internal-to-drop liquid accelerations can be re-scaled as discussed in §7 to unify deformation and breakup times.

Now the essential differences found between C-D3 and C-D0 experiments can be understood with the help of figures 17 and 18. In figure 17, we can contrast the well-organized flow field in C-D3 (recall the smooth highly reproducible development of the drop deformation and breakup patterns in it), against the unsteady character in the C-D0. The latter is further illustrated by the oscillatory character of the lift coefficient, indicating a sideways forcing of the same order of magnitude as the flow dynamic pressure (figure 18). Moreover, in figure 17, we find that the peak in normal stress on the sphere reaches the flow stagnation pressure (as on the front of the cylinder). Thus, as found experimentally, there is no need to rescale the We (breakup is seen at $We_{CR} \sim 10$), and flattening occurs by an equivalent of ‘left–right-punches’ in fast succession that lead to rapid and chaotic breakup. Thus, at the same We , the resulting particle-size distributions are different from those found in isolated drops (RTP, figure 5).

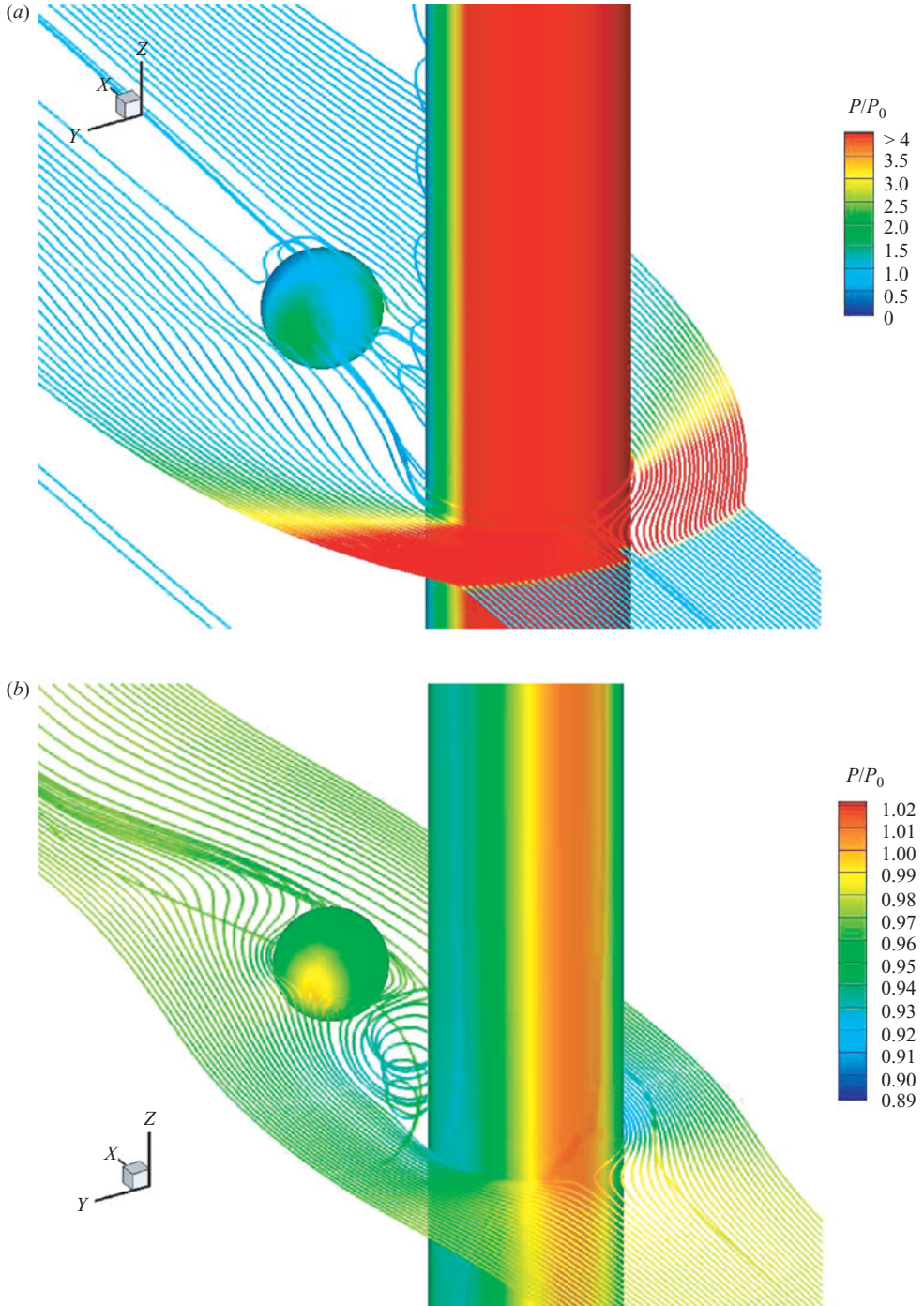


FIGURE 17. Sample representations of the P /streamline patterns in (a) C-D3 and (b) C-D0 conditions. The C-D3 pattern is steady, the C-D0 is unsteady and the illustration is at a time that the pressure on the forward stagnation point of the sphere has a maximum value (it is used as the reference value in the plot).

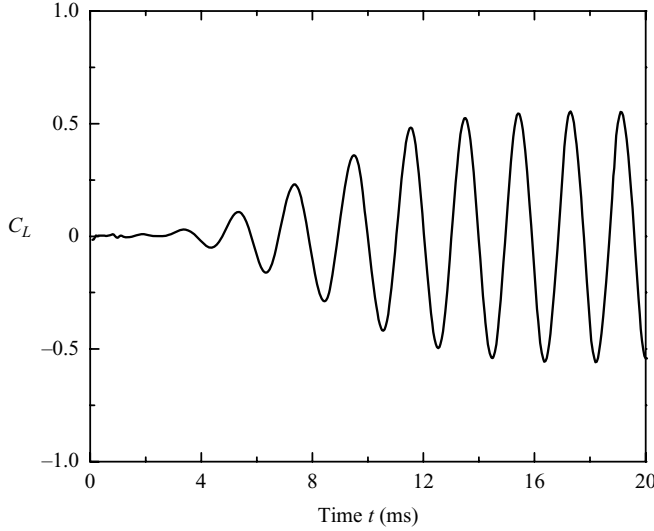


FIGURE 18. The dynamics of sideways forcing on a trailing sphere located at $L_x/D = 2$ in C-D0 type flow.

7. Deformation physics and relevant time scales

In this section, we present the deformation-histories and breakup-time data from our experiments. We shall use a time-scaling procedure similar to that first carried out by Burgers (1958), as presented in Engel (1958), except for paying closer attention to the actual liquid-internal pressure gradients. These gradients can be visualized from the pressure fields obtained by solving Laplace's equation in a sphere, subject to the boundary pressures found in the various cases examined in §6 (figure 19). Note the significantly different distributions between all three cases, and this is important to be accounted for as explained below. While directly relevant to deformation, we expect this scaling to be useful also for breakup, as for this low to medium range of We these two processes are intimately connected (§7.2).

To linear approximation, the drop deformation dynamics are controlled by:

$$\rho_l \frac{\partial U_{l,i}}{\partial t} = -\frac{\partial p}{\partial x_i} \quad \frac{\partial U_{l,i}}{\partial x_i} = 0 \quad \text{subject to } p = P + \sigma\kappa \text{ on the boundary} \quad (7.1)$$

(the capillary pressure is (30, 70) Pa for (TBP, water) at the initial curvature of the drop) where l stands for liquid, p is the pressure in the liquid, κ is the locally-averaged curvature, and the P is the distribution imposed from the aerodynamics. Thus a characteristic acceleration can be written as

$$a = \frac{P_{max} - P_{min}}{\rho_l \Delta L}, \quad (7.2)$$

where ΔL is the distance between the min/max points on the surface. On this basis, the characteristic time for deformation can be expressed in terms of the previously known quantity, t^+ , appearing in (2.4) by:

$$t_D^+ \sim \sqrt{\frac{\Delta L}{a}} \sim \left\{ \frac{\Delta L}{d} \sqrt{\frac{2}{C}} \right\} \frac{d}{u} \sqrt{\frac{\rho_l}{\rho_g}} \equiv C_t t^+, \quad (7.3)$$

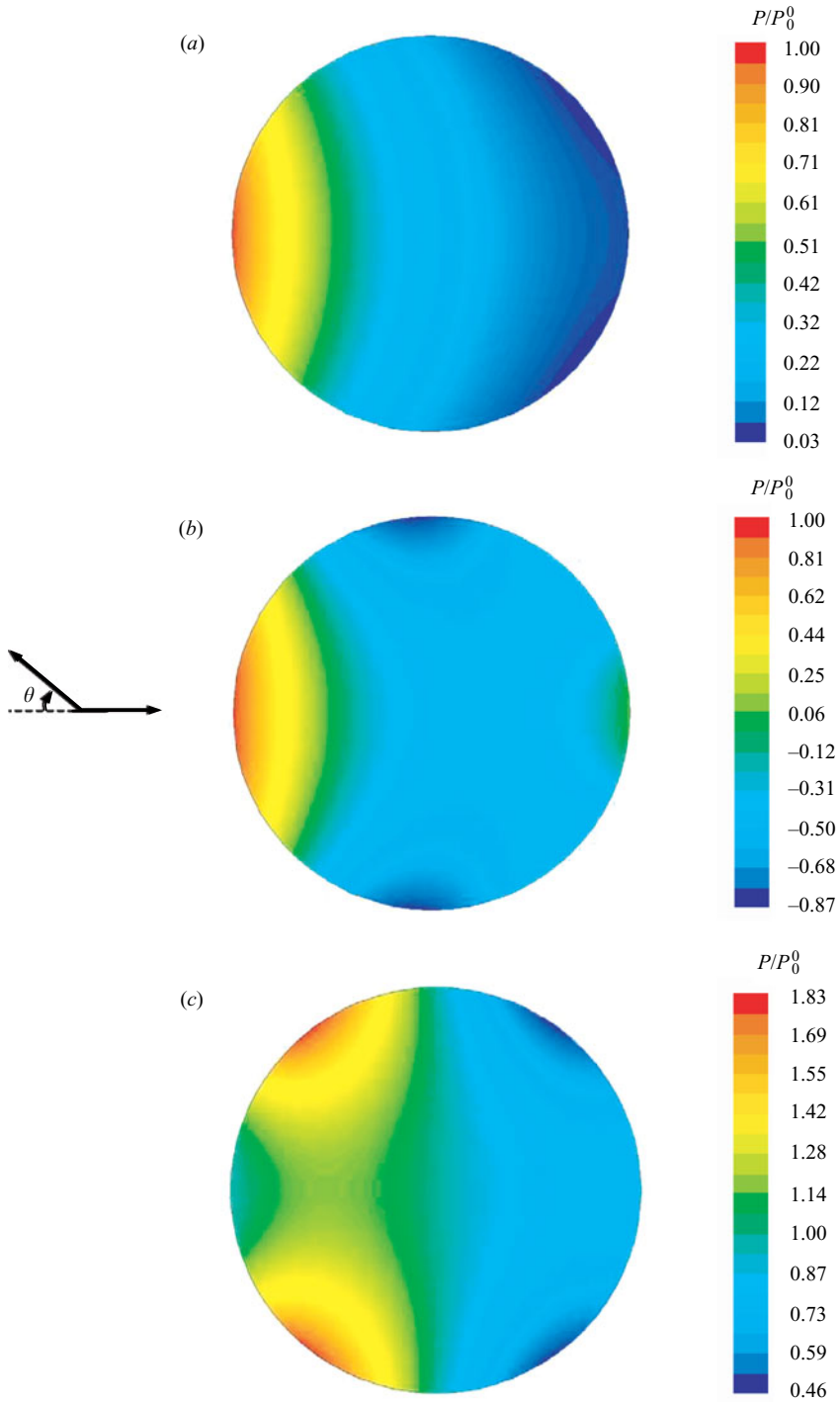


FIGURE 19. Pressure field in diametral (parallel-to-the-flow, normal-to-the-cylinder) plane through the drop. (a) D3, $P_0^0 = 550$ Pa, (b) D0, $P_0^0 = 307$ Pa (P is gauge pressure), (c) C-D3.A, $P_0^0 = 53$ Pa, where P_0^0 is the pressure at $\theta = 0$.

<i>Isolated drop in supersonic flow (D3)</i>									
	We	$\frac{1}{2}\rho_g u^2$ (Pa)	$\frac{2P_{max}}{\rho_g u^2}$	θ_{max} (deg.)	$\frac{2P_{min}}{\rho_g u^2}$	θ_{min} (deg.)	$\frac{\Delta L}{d}$	C	C_t
	80	287	1.89	0	0.06	± 144	0.95	1.83	0.99
	150	539	2.05	0	0.06	± 138	0.93	1.99	0.93
<i>Isolated drop in subsonic flow (D0)</i>									
	We	$\frac{1}{2}\rho_g u^2$ (Pa)	$\frac{2P_{max}}{\rho_g u^2}$	θ_{max} (deg.)	$\frac{2P_{min}}{\rho_g u^2}$	θ_{min} (deg.)	$\frac{\Delta L}{d}$	C	C_t
	28	292	1.01	0	-0.88	± 84	0.67	1.89	0.69
<i>Cylinder-drop geometry in supersonic flow (C-D3)</i>									
$\frac{L_x}{D}$	We	$\frac{1}{2}\rho_g u^2$ (Pa)	$\frac{2P_{max}}{\rho_g u^2}$	θ_{max} (deg.)	$\frac{2P_{min}}{\rho_g u^2}$	θ_{min} (deg.)	$\frac{\Delta L}{d}$	C	C_t
2	80	287	0.33	± 50	0.08	± 125	0.74	0.25	1.71
2	150	539	0.37	± 50	0.08	± 125	0.70	0.29	1.61
4	80	287	0.44	± 33	0.06	± 129	0.74	0.38	1.70
4	150	539	0.47	± 36	0.05	± 126	0.71	0.41	1.56
10	80	287	0.68	0	0.04	± 132	0.91	0.64	1.62
10	150	539	0.63	0	0.04	± 129	0.90	0.59	1.66

TABLE 3. Summarization of computational results for the quantification of coefficients C and C_t . (P_{max} , P_{min}) are absolute pressures for the supersonic flows, and gauge pressures for the subsonic flow. These results were also independently obtained (in a previous study) by the commercial CFD code FLUENT, and were found to be essentially the same: $45 < We < 491$ (for the D3 case), $7 < We < 100$ (for the D0 case), and $45 < We < 300$ (for the C-D3 case).

where C is a pressure coefficient defined by

$$C = \frac{P_{max} - P_{min}}{0.5\rho_g u^2}, \quad (7.4)$$

and available from the simulations in §6. The results for C and C_t are summarized in table 3 and are used in the following.

7.1. Deformation-time data

Deformation-history data were deduced from measurement of cross-stream and streamwise dimensions of the drops for as long as they remained coherent. For the isolated-drop data, we found that the ratio of these two quantities provides a sensitive measure of the deformation dynamics. The data from Theofanous & Li (2007) are shown in this manner in figure 20. For the C-D3 runs, since the streamwise dimension increases as well, a better representation of deformation is obtained from the relative increase in the cross-stream direction – the data from Series A are shown in figure 21. In both figures, time was non-dimensionalized by means of (7.3) incorporating numerical results in table 3. Clearly, this is effective to ‘collapse’ the data, and to show a universal deformation time, T_D , (at which peak deformation is reached):

$$T_D = \frac{t_D}{t_D^+} \sim 1, \quad (7.5)$$

for wide ranges of flow parameters and free as well as obstructed geometries.

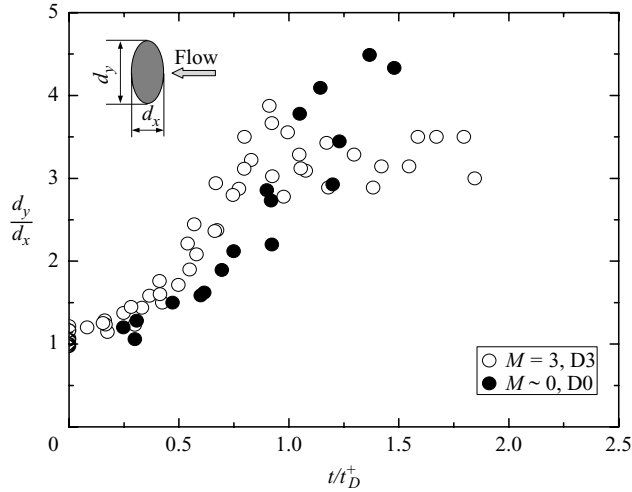


FIGURE 20. Scaled representation of drop-deformation histories in subsonic and supersonic flow. d_y is the drop diameter in the direction normal to the flow, d_x is the liquid thickness in the flow direction.

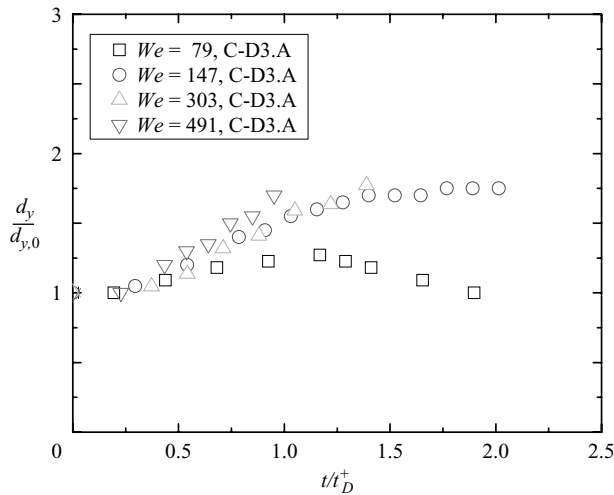


FIGURE 21. Scaled representation of drop-deformation histories in C-D3 type flow. d_y is drop diameter in the direction normal to the flow, subscript 0 denotes initial value.

7.2. Breakup-time data

The definition of drop-breakup time in the literature is burdened by significant ambiguity; much of it derived from differing interests in applications, but much of it also being due to visualization difficulties. These arise at the intense fine-scale mixing found in high- We interactions, and associated multiple light refractions that quickly obscure the view in the shadowgraph method (see figure 7). For example, in early work, the interest was on the time required for complete drop annihilation; that is, conversion into a diffuse micro-mist that would be benign to the frontal area of re-entry vehicles (Waldmann *et al.* 1972). Other applications in subsequent work, such as multiphase combustion, would appear open to benefit from more detailed

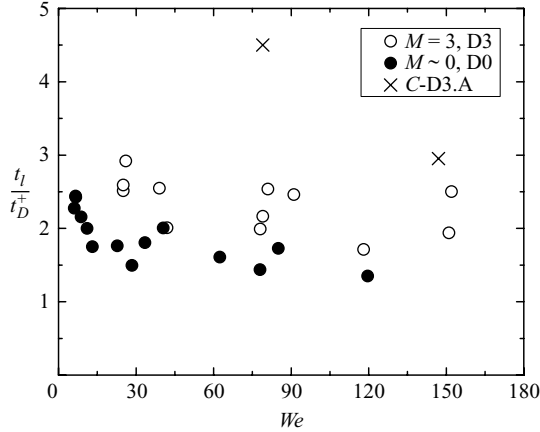


FIGURE 22. Scaled representation of initial-breakup times for all flow conditions.

definitions, but perhaps owing to the visualization difficulties just mentioned they were not pursued. As a result, a ‘standard’ rule-of-thumb evolved for breakup-time, t_B , defined on the diffuse micromist idea as:

$$T_B = \frac{t_B}{t^+} \sim 5. \quad (7.6)$$

This is an empirical result, the principal bases of which are the shadowgraphy data of Ranger & Nicholls (1969) and the X-radiography data of Rienecke *et al.* (1975) for flows up to Mach 3. This is in approximate agreement with all our data as well.

In the present work, we are more interested in the complete dynamics of breakup, and as additional measures for this purpose we will adopt the time for initiation of entrainment, t_I , and the time that marks complete loss of coherence, t_{LC} . The t_I is easy to measure with high accuracy, even in shadowgraphs. In the present experiments the t_{LC} is also clear, and now, with LIF (figures 5–7), this can be also discerned accurately for isolated drops even at intermediate Weber numbers (Theofanous & Li 2007). For example, the t_I in C-D3.A(79) (figure 24), is taken as 38.4 ms, while the t_{LC} in C-D3.A(147) (figure 25) is taken as $t = 11.1$ to 13.9 ms. The results from representative C-D3, D3 and D0 runs are summarized in figures 22 and 23 and indicate that for this low-to-medium range of We examined

$$T_I \sim T_{LC} \sim 2 \text{ to } 3. \quad (7.7)$$

8. Conclusions

The presence of obstacles alters radically the mechanisms and patterns of aerobreakup. Supersonic flows in the presence of a cylindrical obstacle reveal amazingly rich morphologies, all sensitive to the value of We , but perfectly regular and reproducible in fine detail. Subsonic flows yield similar general behaviours but now patterns are unstable and chaotic. Two-drop configurations in subsonic flows yield even more rich morphologies; they are more variable in complexity as patterns now evolve in a highly interactive manner. The general effect is planar or centripetal squeeze (deformation), depending on the geometry of the obstacle and the magnitude of We . In all cases, these effects begin to disappear at some downstream distance of ~ 10 diameters, but in supersonic flow, significant reductions of the effective We is

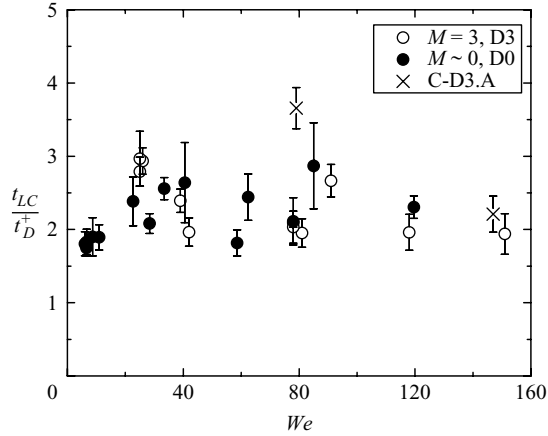


FIGURE 23. Scaled representation of total-loss-of-coherence times for all flow conditions.

seen well past this distance. The highly-resolved complete-sequence images presented in the Appendix lend themselves to testing/benchmarking on numerical simulations of interfacial flows. More specifically, the conclusions can be listed as follows.

1. Sheltered geometries in supersonic flow yield long-range effects that lower the effective We from free-stream values. Thus for the cases considered here, a drop behind a cylindrical obstacle in Mach 3 flow, a free stream $We \sim 10^2$ is required for breakup as compared to $We \sim 10$ for isolated drops.

2. Below the critical value, the drops elongate in the flow direction, above it they flatten on a plane parallel to flow and cylinder-axis directions.

3. Breakup in sheltered supersonic flow conditions is orderly, with intricate interfacial and topological-change patterns that are reproducible in fine detail.

4. Sheltered geometries in subsonic flow are dominated by unsteady vortex-shedding effects, at effective We that are the same as in free stream. Breakup occurs at $We \sim 10$, but instead of the patterns found with isolated drops we have flattening parallel to the flow direction, and the flattened structure is short-lived and disintegrates chaotically.

5. All these effects are shown to be amenable to quantitative interpretation by means of simulations of the aerodynamics in fixed-body geometries. These interpretations include the scaling of deformation and breakup times that conform to those of isolated drops in both subsonic and supersonic flow.

This work was supported by the Joint Science and Technology Center of the Defense Threat Reduction Agency (JSTO/DTRA), Lawrence Livermore National Laboratory (the HOPS program), and the National Ground Intelligence Center (NGIC). The support and collaboration of Drs C. Fromer, J. Hanna, F. Handler, R. Babarsky and G. Nakafuji is gratefully acknowledged. The numerical simulation codes UNCLE and C-UNCLE were developed at the University of Kentucky by Professors G. Huang and R. LeBeau, and we appreciate their cooperation in making them available for this work.

Appendix

Figures 24–27 are complete time-resolved sequences, excerpts of which are shown in figure 9. Similarly figures 28–30 are excerpted in figure 10, and 31–33 in figure 11.

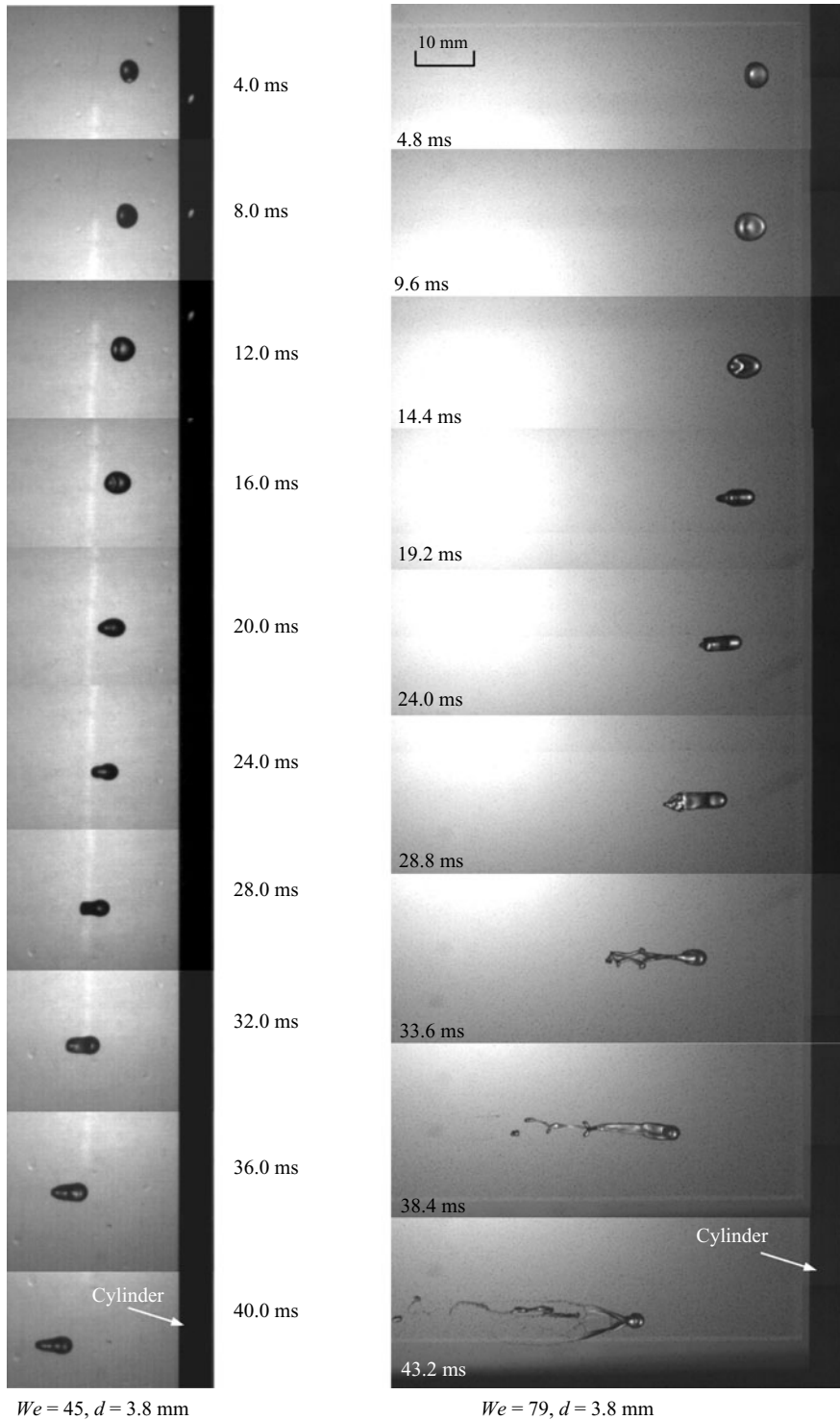


FIGURE 24. C-D3.A(45) and C-D3.A(79). $t^+ = (6.6, 5.0) \text{ ms}$ for $We = (45, 79)$.

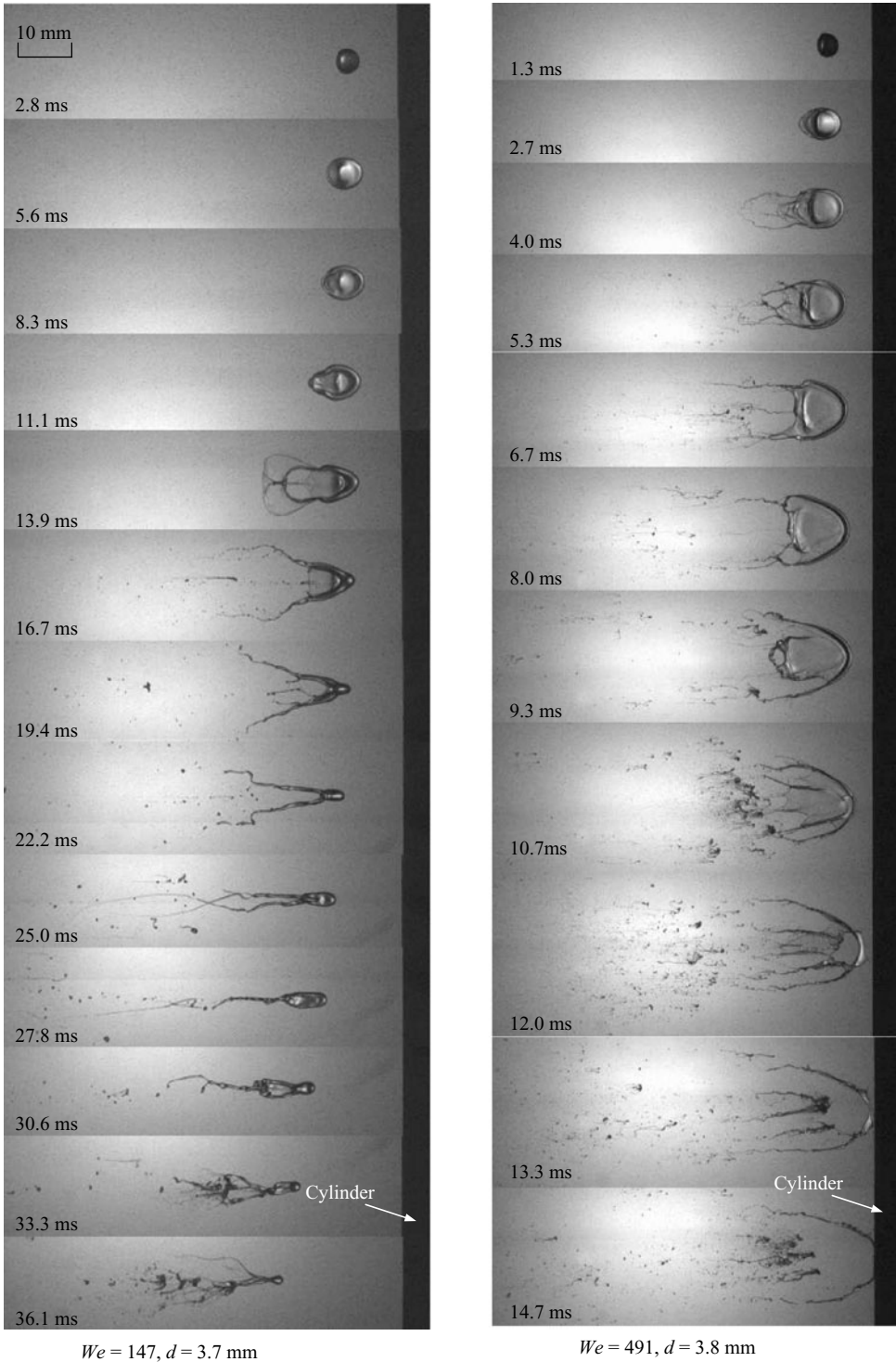


FIGURE 25. C-D3.A(147) and C-D3.A(491). $t^+ = (3.5, 2.0)$ ms for $We = (147, 491)$.

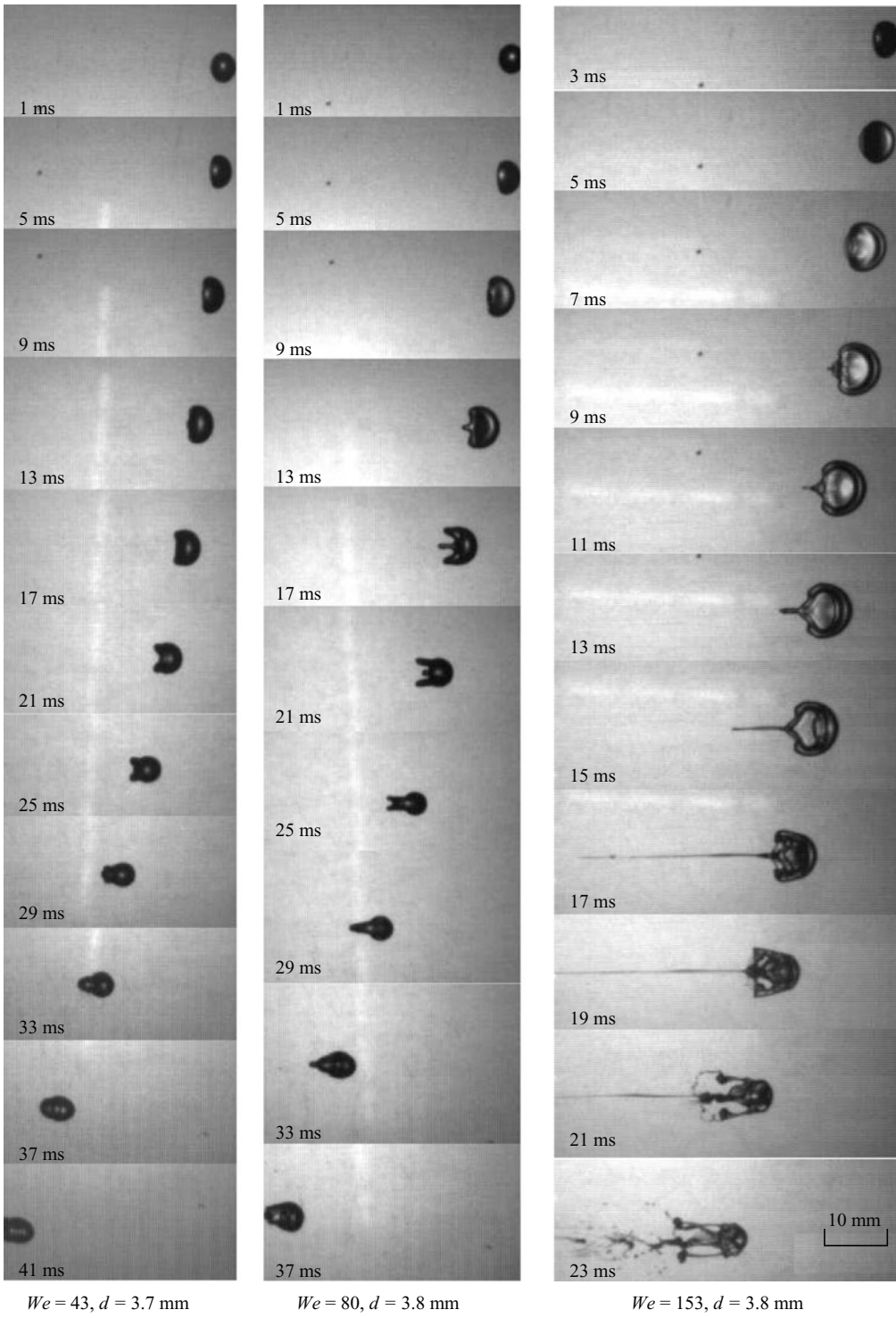
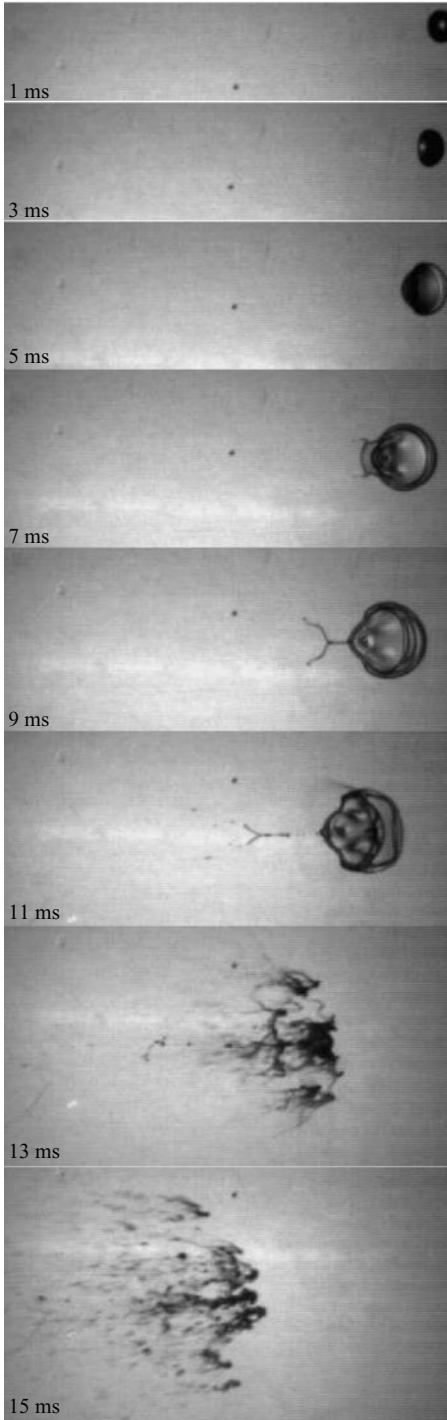
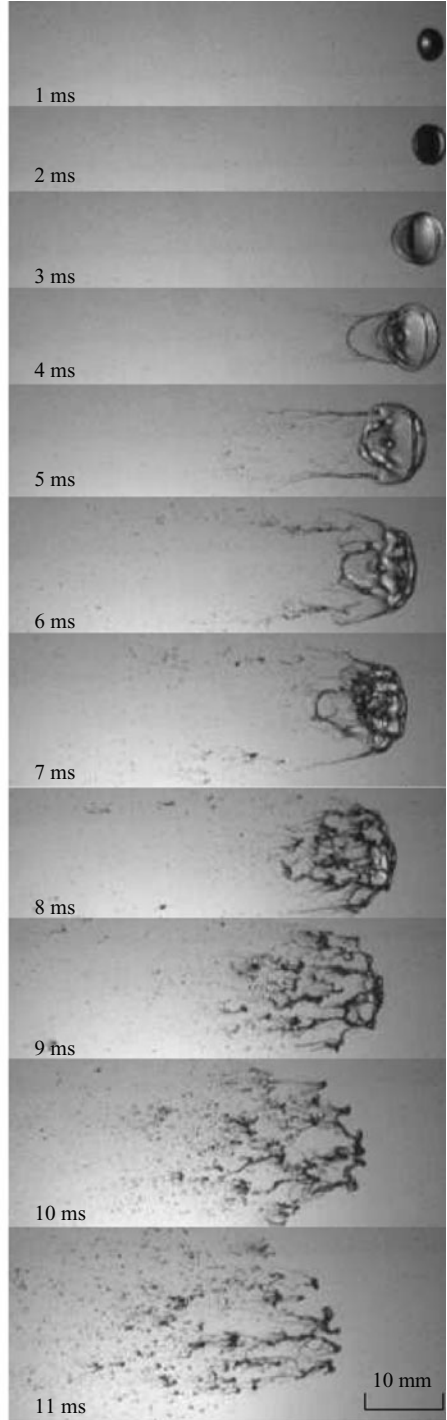


FIGURE 26. C-D3.B(43), C-D3.B(80) and C-D3.B(153) $t^+ = (6.5, 5.0, 3.6)$ ms for $We = (43, 80, 153)$.



$We = 299, d = 3.7 \text{ mm}$



$We = 483, d = 3.7 \text{ mm}$

FIGURE 27. C-D3.B (299) and C-D3.B (483). $t^+ = (2.5, 1.9) \text{ ms}$ for $We = (299, 483)$.

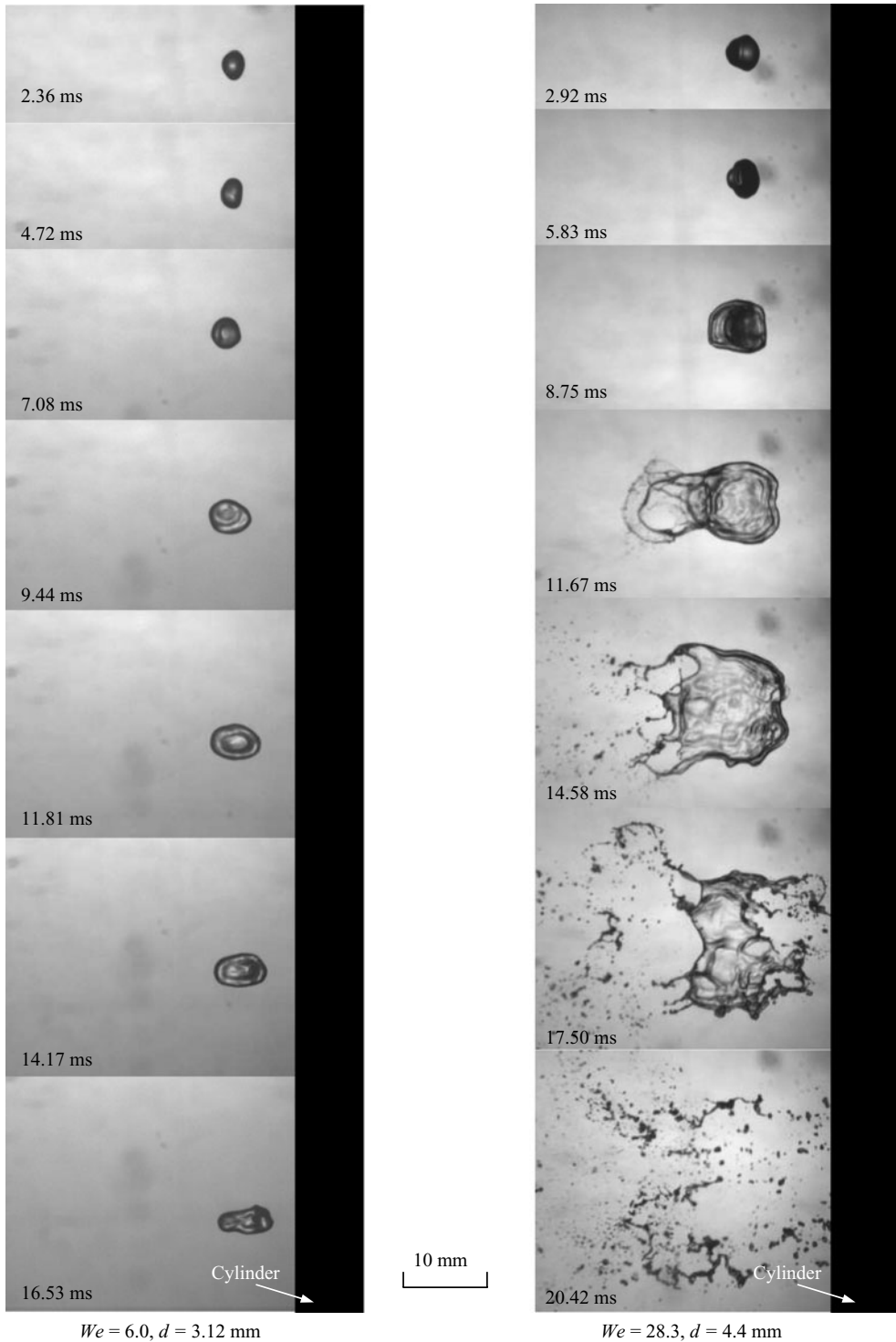
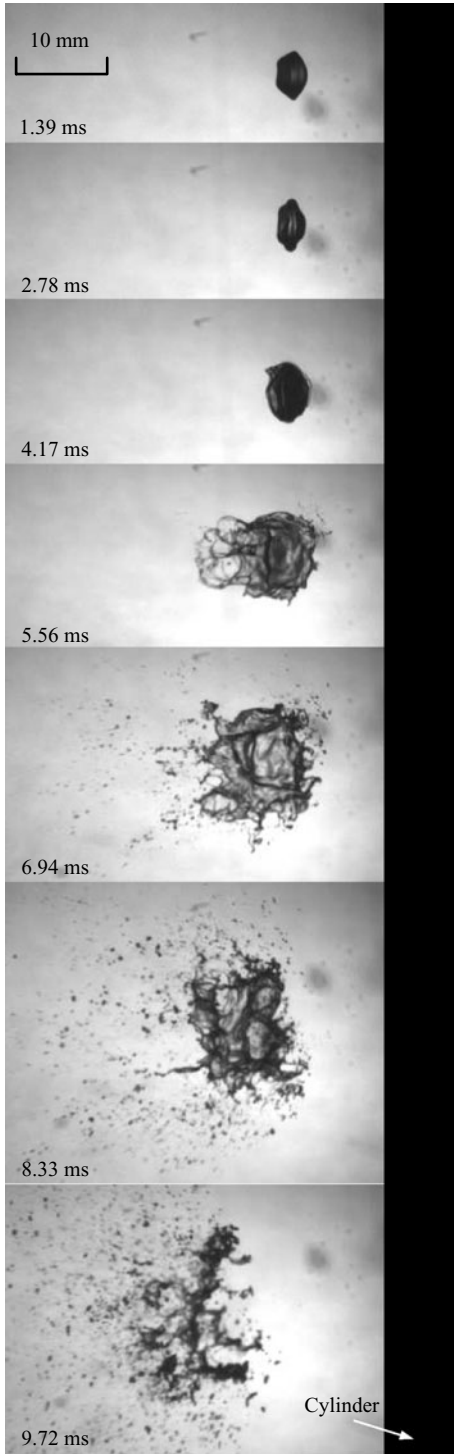
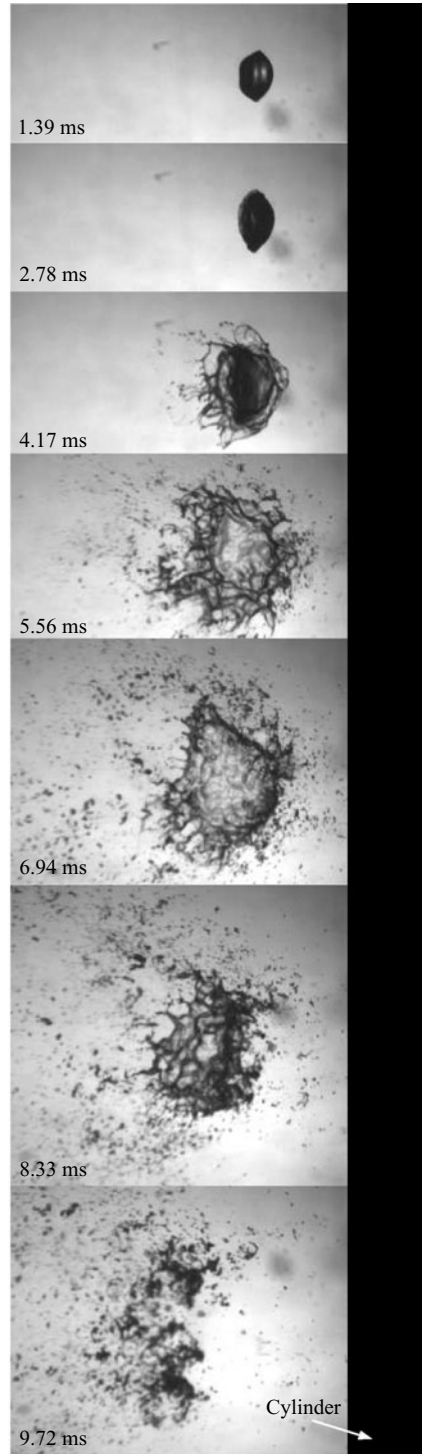


FIGURE 28. C-D0.A(6) and C-D0.A(28.3). $t^+ = (8.5, 6.5)$ ms for $We = (6, 28.3)$.



$We = 76.0, d = 4.31 \text{ mm}$



$We = 121.2, d = 4.49 \text{ mm}$

FIGURE 29. C-D0.A(76) and C-D0.A(121). $t^+ = (3.9, 3.3) \text{ ms}$ for $We = (76, 121)$.

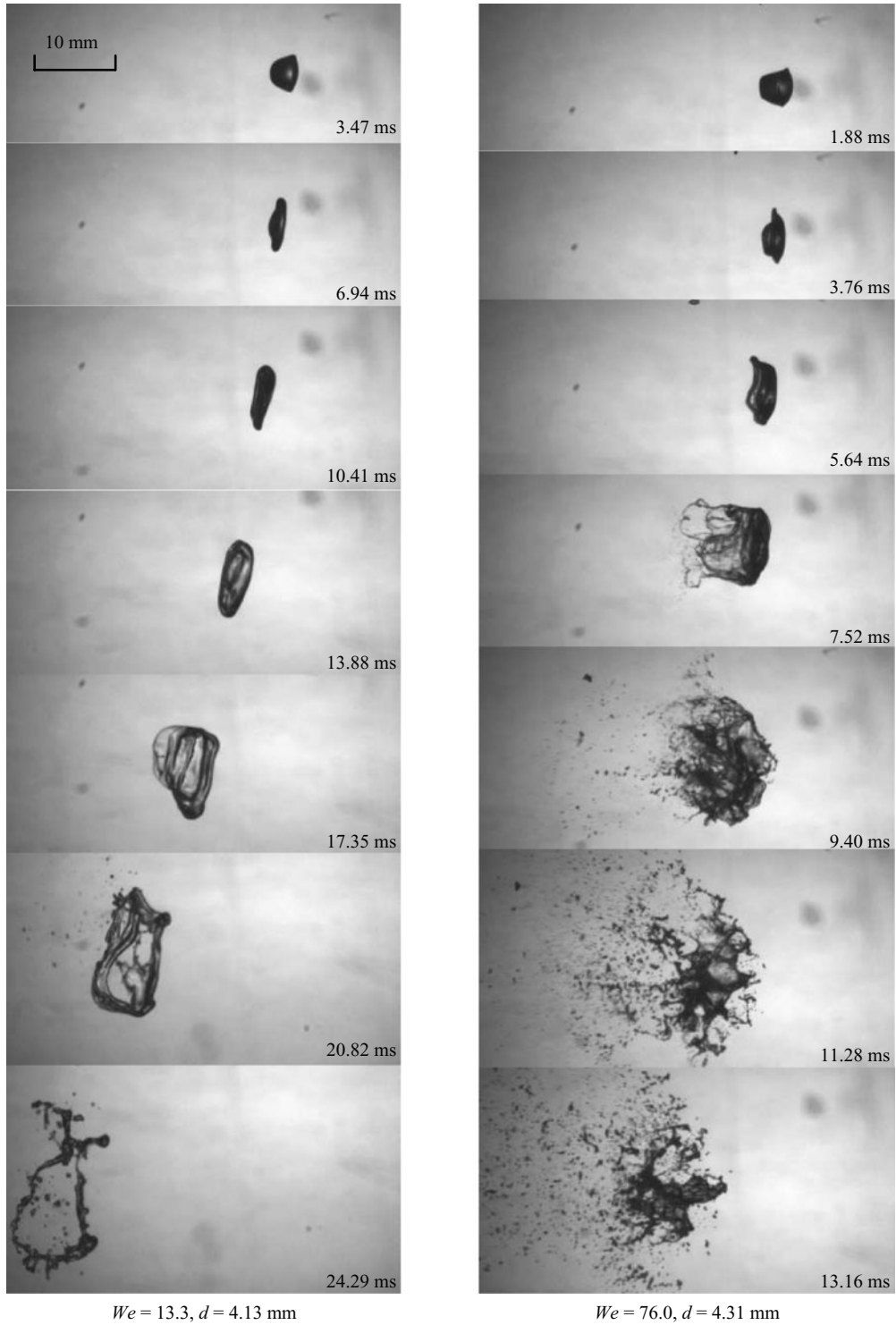
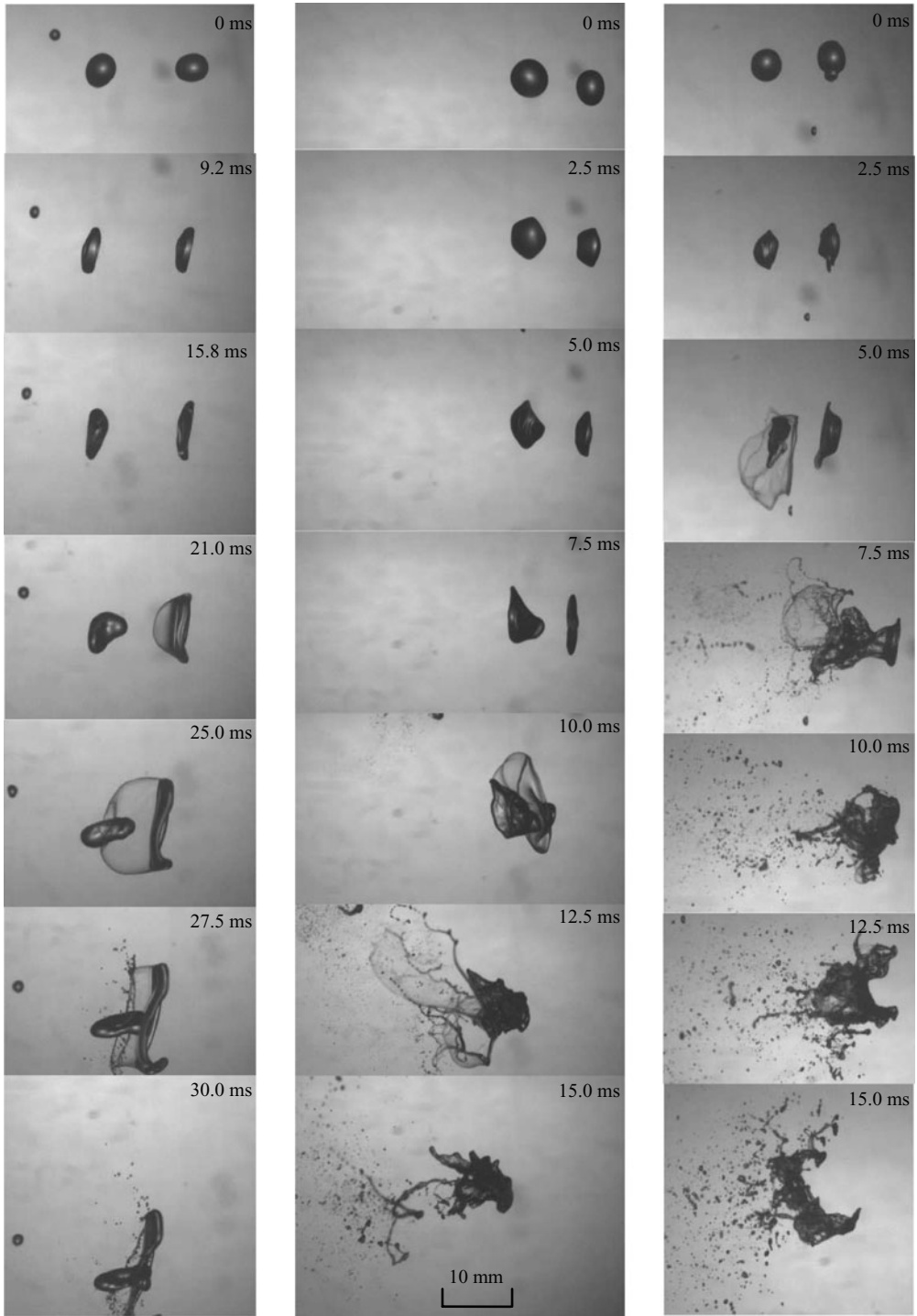


FIGURE 30. C-D0.B(13.3) and C-D0.B(76). $t^+ = (8.7, 3.9)$ ms for $We = (13.3, 76)$.



$L_y/d_1 = 3, We = 6.0$

$L_y/d_1 = 2, We = 17.0$

$L_y/d_1 = 2, We = 32.3$

FIGURE 31. D-D0.A(6), D-D0.A(17) and D-D0.A(32.3). $\tau^+ = (16.2, 9.4, 6.3)$ ms for $We = (6, 17, 32.3)$.

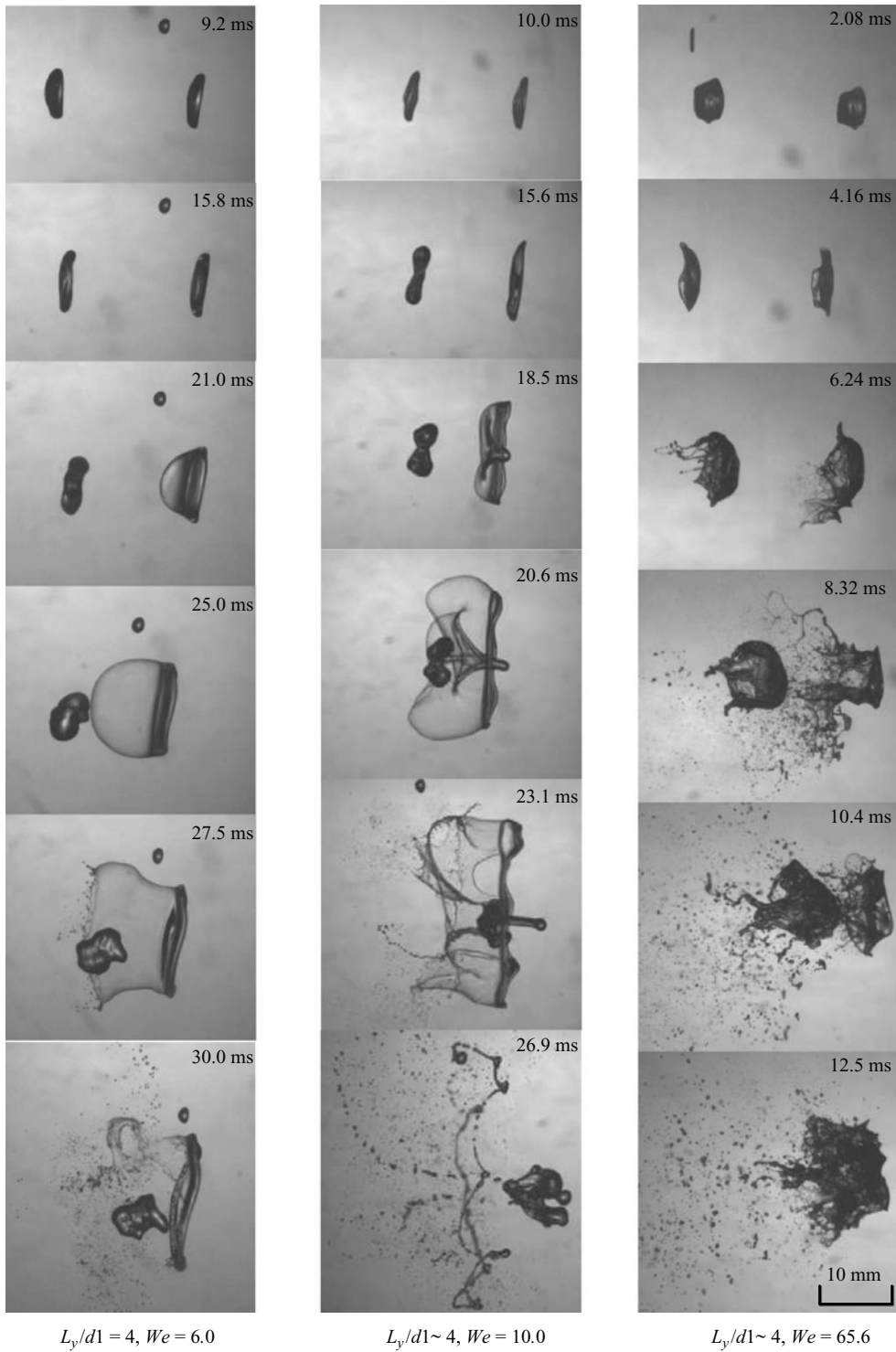
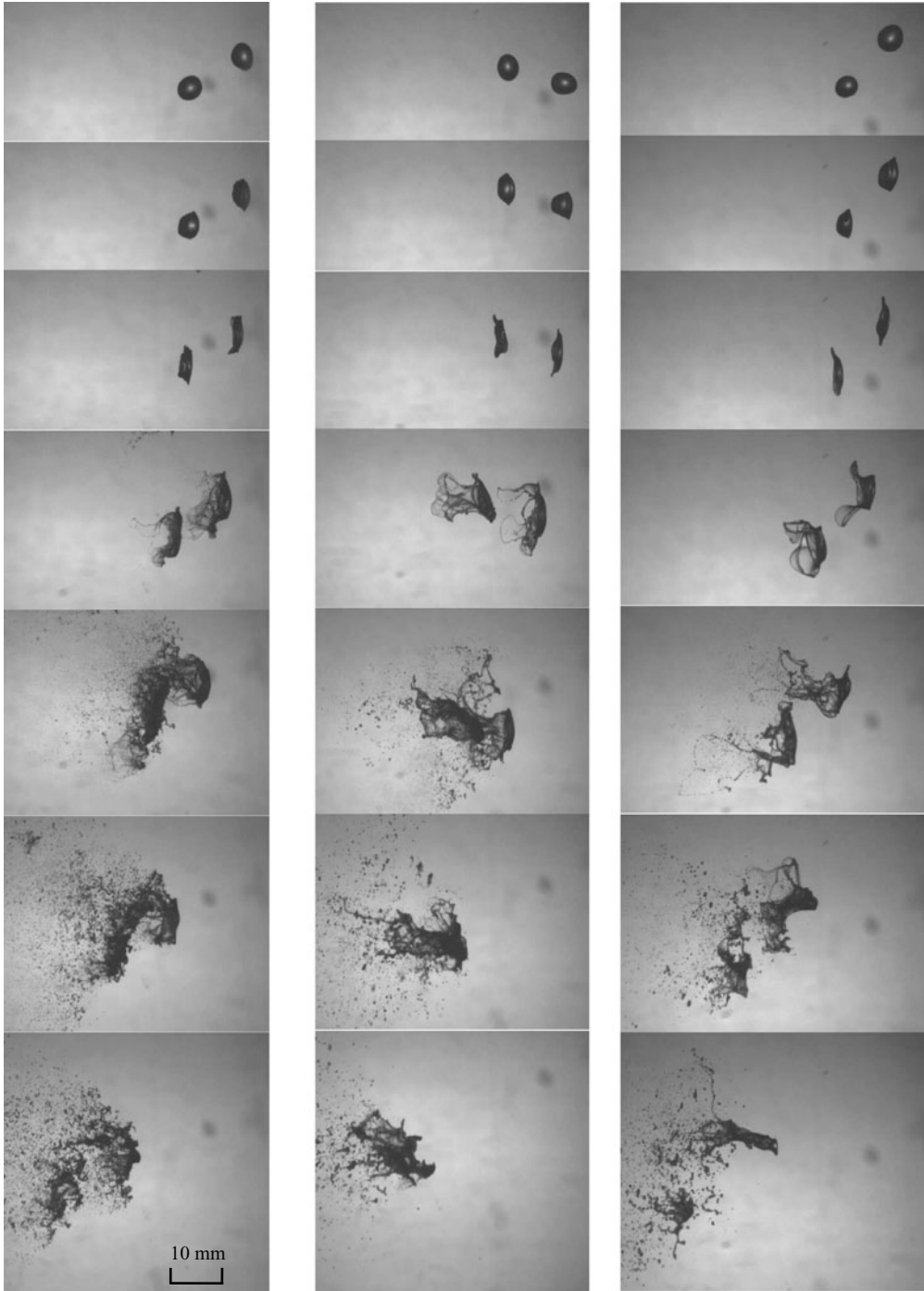


FIGURE 32. D-D0.B(6), D-D0.B(10) and D-D0.B(65.6). $t^+ = (16.6, 14.0, 5.3)$ ms for $We = (6, 10, 65.6)$.



$L_y/d1 = 2, L_x/d1 = 1$
 $We = 125$

Time interval: 1.88 ms

$L_y/d1 = 2, L_x/d1 \sim 1$
 $We = 62.0$

Time interval: 1.88 ms

$L_y/d1 = 2, L_x/d1 = 1$
 $We = 32.3$

Time interval: 1.88 ms

FIGURE 33. D-D0.D (125), D-D0.D(62) and D-D0.D(32.3). $t^+ = (3.5, 4.8, 6.3)$ ms for $We = (125, 62, 32.3)$.

REFERENCES

- BAILEY, A. B. & HIATT, J. 1972 Sphere drag coefficients for a board range of Mach and Reynolds number. *AIAA J.* **10**, 1436–1440.
- BRODKEY, R. 1969 *The Phenomena of Fluid Motions*. Reading, MA.
- BURGERS, J. M. 1958 *J. Res. Natl Bur. Stand.* **60**, 278.
- CHAKRAVARTHY, S. R. & OSHER, S. 1985 Computing with high-resolution upwind schemes for hyperbolic equation. *Lect. Appl. Maths* **22**, 57–86.
- CHEN, H., LEBEAU, R. P. & HUANG, P. G. 2005 A cell-centered ressure based method for unstructured incompressible Navier–Stokes solvers. *43rd AIAA Aerospace Sciences Meeting and Exhibit AIAA-2005-0880, Reno, NV, January 10–13, 2005*.
- CHOU, W.-H. & FAETH, G. M. 1998 Temporal properties of secondary drop breakup in the bag breakup regime. *Intl J. Multiphase Flow* **24**, 889–912.
- CHOU, W.-H., HSIANG, L. P. & FAETH, G. M. 1997 Temporal properties of drop breakup in the shear breakup regime. *Intl J. Multiphase Flow* **23**, 651–669.
- DAI, Z. & FAETH, G. M. 2001 Temporal properties of secondary drop breakup in the multimode breakup regime. *Intl J. Multiphase Flow* **27**, 217–236.
- ENGEL, O. G. 1958 Fragmentation of water drops in the zone behind an air shock. *J. Res. Natl Bur. Stand.* **60**, 245–280.
- GEL'FAND, B. E. 1996 Droplet breakup phenomena in flows with velocity lag. *Prog. Energy Combust. Sci.* **22**, 201–265.
- GEL'FAND, B. E., GUBIN, S. A. & KOGARKO, S. M. 1974 Various forms of drop fractionation in shock waves and their special characteristics. *InZh.-Fizich. Zhurnal* **27**, 119–126.
- HANSON, A. R., DOMICH, E. G. & ADAMS, H. S. 1963 Shock tube investigation of the breakup of drops by air blasts. *Phys. Fluids* **6**, 1070–1080.
- HARPER, E. Y., GRUBE, G. W. & CHANG, I.-D. 1972 On the breakup of accelerating liquid drops. *J. Fluid Mech.* **52**, 565–591.
- HINZE, J. O. 1955 Fundamentals of the hydrodynamic mechanism of splitting in dispersion processes. *AICHE J.* **1**, 289–295.
- HSIANG, L.-P. & FAETH, G. M. 1992 On the breakup of accelerating liquid drops. *Intl J. Multiphase Flow* **18**, 635–652.
- JOSEPH, D. D., BELANGER, J. & BEAVERS, G. S. 1999 Breakup of a liquid suddenly exposed to a high-speed airstream. *Intl J. Multiphase Flow* **25**, 1263–1303.
- JOSEPH, D. D., BEAVERS, G. S. & FUNADA, T. 2002 Rayleigh–Taylor instability of viscoelastic drops at high Weber numbers. *J. Fluid Mech.* **453**, 109–132.
- LI, G. J., SUSHCHIKH, S. Y., NOURGALIEV, R. R., DINH, T. N. & THEOFANOUS, T. G. 2003 Detailed characterization of the gas dynamics in the ALPHA facility. CRSS Report, CRSS-03/08.
- LIEPMANN, H. W. & ROSHKO, A. 1957 *Elements of Gasdynamics*. John Wiley.
- LIU, M.-S. 1996 A sequel to *AUSM*: *AUSM*⁺. *J. Comput. Phys.* **129**, 364–382.
- MASLACH, G. J. & SCHAAF, S. A. 1963 Cylinder drag in the transition from continuum to free molecule flow. *Phys. Fluids* **6**, 315–321.
- MATTA, J. E. & TYTUS, R. P. 1982 Viscoelastic breakup in a high velocity airstream. *J. Appl. Polymer Sci.* **27**, 397–405.
- NOURGALIEV, R. R. & THEOFANOUS, T. G. 2007 High-fidelity interface tracking in compressible flows: unlimited anchored adaptive Level Set. *J. Comput. Phys.* **224**, 836–866.
- NOURGALIEV, R. R., DINH, T. N. & THEOFANOUS, T. G. 2006 Adaptive characteristics-based matching for compressible multifluid dynamics. *J. Comput. Phys.* **213**, 500–529.
- NOURGALIEV, R. R., LIU, M.-S. & THEOFANOUS, T. G. 2007 Numerical prediction of interfacial instabilities: sharp interface method (SIM). *J. Comput. Phys.* (submitted).
- RANGER, A. A. & NICHOLLS, J. A. 1969 Aerodynamic shattering of liquid drops. *AIAA J.* **7**, 285–290.
- REINECKE, W. & WALDMAN, G. D. 1970 A study of drop breakup behind strong shocks with applications to flight. Final report, AVCO Government Products Report, SAMCO-TR-70-142.
- REINECKE, W. G. WANDMAN, G. D. MCKAY, L. W. L. & ZIERING, M. B. 1975 Shock layer shattering of water drops and ice crystals in reentry flight. Final Report, AVCO Government products report, AFML-TR-75-71.

- SIMPKINS, P. G. & BALES, E. L. 1972 Water-drop response to sudden accelerations. *J. Fluid Mech.* **55**, 629–639.
- TAYLOR, G. I. 1949 The shape and acceleration of a drop in a high-speed air stream. In *The Scientific Papers of G. I. Taylor* (ed. G. K. Batchelor). Cambridge University Press.
- THEOFANOUS, T. G. 2005 Source term for atmospheric dispersal of liquid agents. *Defense Threat Reduction Agency's Science & Technology Conference on Chemical and Biological Information Systems, Albuquerque, New Mexico, Oct. 25–28, 2005*.
- THEOFANOUS, T. G. & LI, G. J. 2007 On the physics of aero-breakup. *Phys. Fluids* (in press)
- THEOFANOUS, T. G., LI, G. J. & DINH, T. N. 2004 Aerobreakup in rarefied supersonic flows. *Trans. ASME J: J. Fluids Engng* **126**, 516–527.
- THEOFANOUS, T. G., NOURGALIEV, R. R., LI, G. J. & DINH, T. N. 2006 Compressible multi-hydrodynamics (CMH): breakup, mixing, and dispersal, of liquids/solids in high speed flows. In *Proc. IUTAM Symp. on Computational Approaches to Disperse Multiphase flow* (ed. A. Prosperetti & S. Balachandar). Springer.
- VILLERMAUX, E., MARMOTTANT, PH. & DUPLAT, J. 2004 Ligament-mediated spray formation. *Phys. Rev. Lett.* **92**, 07405-1–4.
- WALDMAN, G. D., REINECKE, W. & GLENN, D. C. 1972 Raindrop breakup in the shock layer of a high-speed vehicle. *AIAA J.* **10**, 1200–1204.